

Efficiently Improving Ensemble Forecasts of Warm-Sector Heavy Rainfall over Coastal Southern China: Targeted Assimilation to Reduce the Critical Initial Field Errors

Xinghua BAO¹, Rudi XIA^{1,2*}, Yali LUO^{1,2}, and Jian YUE^{3,1}

¹ State Key Laboratory of Severe Weather, Chinese Academy of Meteorological Sciences (CAMS), China Meteorological Administration (CMA), Beijing 100081

² Collaborative Innovation Center on Forecast and Evaluation of Meteorological Disasters (CIC-FEMD), Nanjing University of Information Science & Technology, Nanjing 210044

³ CMA Earth System Modeling and Prediction Centre, China Meteorological Administration, Beijing 100081

(Received 19 September 2022; in final form 29 March 2023)

ABSTRACT

Warm-sector heavy rainfall events over southern China are difficult to accurately forecast, due in part to inaccurate initial fields in numerical weather prediction models. In order to determine an efficient way of reducing the critical initial field errors, this study conducts and compares two sets of 60-member ensemble forecast experiments of a warm-sector heavy rainfall event over coastal southern China without data assimilation (NODA) and with radar radial velocity data assimilation (RadarDA). Yangjiang radar data, which can provide offshore high-resolution wind field information, were assimilated by using a Weather Research and Forecasting (WRF)-based ensemble Kalman filter (EnKF) system. The results show that the speed and direction errors of the southeasterly airflow in the marine boundary layer over the northern South China Sea may primarily be responsible for the forecast errors in rainfall and convection evolution. Targeted assimilation of radial velocity data from the Yangjiang radar can reduce the critical initial field errors of most members, resulting in improvements to the ensemble forecast. Specifically, RadarDA simulations indicate that radial-velocity data assimilation (VrDA) can directly reduce the initial field errors in wind speed and direction, and indirectly and slightly adjust the initial moisture fields in most members, thereby improving the evolution features of moisture transport during the subsequent forecast period. Therefore, these RadarDA members can better capture the initiation and development of convection and have higher forecast skill for the convection evolution and rainfall. The improvement in the deterministic forecasts of most members results in an improved overall ensemble forecast performance. However, VrDA sometimes results in inappropriate adjustment of the initial wind field, so the forecast skill of a few members decreases rather than increases after VrDA. This suggests that a degree of uncertainty remains about the effect of the WRF-based EnKF system. Moreover, the results further indicate that accurate forecasts of the convection evolution and rainfall of warm-sector heavy rainfall events over southern China are challenging.

Key words: ensemble forecast, targeted assimilation, warm-sector heavy rainfall

Citation: Bao, X. H., R. D. Xia, Y. L. Luo, et al., 2023: Efficiently improving ensemble forecasts of warm-sector heavy rainfall over coastal southern China: Targeted assimilation to reduce the critical initial field errors. *J. Meteor. Res.*, **37**(4), 486–507, doi: 10.1007/s13351-023-2140-8.

1. Introduction

The first scientific field campaign on pre-summer heavy rainfall (HR) in southern China during 1977–1981 revealed the characteristics of warm-sector HR in the region (Compiling Group of Rainstorm in South China's Pre Flood Season, 1986). Since then, many studies have

been devoted to clarifying the mechanisms of the warm-sector HR. Due to the suddenness and strong intensity of warm-sector HR, operational global and regional numerical weather prediction (NWP) models have low forecast skill for this phenomenon (Ding, 1994; Huang and Luo, 2017; Luo et al., 2017; Wu N. G. et al., 2020).

The warm-sector HR often occurs under weak synop-

Supported by the National Key Research and Development Program of China (2022YFC3003903), National Natural Science Foundation of China (42030610 and 41774002), Science and Technology Development Fund of CAMS (2019KJ018), and Basic Research Fund of CAMS (2023Z008, 2023Z001, and 2023Z020).

*Corresponding author: xiard@cma.gov.cn

© The Chinese Meteorological Society and Springer-Verlag Berlin Heidelberg 2023

tic-scale forcing, with no fronts nearby or within 200 km. The frequency of warm-sector HR in coastal southern China is higher than that in the inner mainland (Li and Du, 2021). The mechanism of warm-sector HR in coastal areas is more complicated due to the complex underlying surface. Numerous studies have revealed that the warm-sector HR in coastal southern China is caused by multi-scale atmospheric processes and is affected by many factors, such as the low-level jet (Du and Chen, 2018, 2019), coastline, terrain (Du et al., 2020b), meso-scale cold pool (Liu et al., 2018), and urban heat island effect (Wu et al., 2019; Yin et al., 2020; Sun et al., 2021). The boundary layer (BL) flow originating from tropical areas, especially the boundary layer jet (BLJ), has been emphasized as playing a crucial role in the initiation of warm-sector HR (Luo et al., 2017, 2020; Du et al., 2020a). The intensity, location, and morphology of the BLJ can affect the time and location of convective initiation and the morphology and evolution of HR-producing convective systems through continuous moisture and energy transport to coastal southern China. Specifically, the warm-sector HR tends to reach a maximum under a moderate BLJ rather than under a strong BLJ (Du et al., 2022).

There is a strong correlation between the NWP skill for the warm-sector HR in coastal southern China and the forecast accuracy of BL airflows. Zhang and Meng (2019) demonstrated that the Weather Research and Forecasting (WRF) model simulations tend to overestimate the coastal planetary BL (PBL) wind, thereby greatly underestimating the coastal precipitation. As NWP has an initial value problem in its mathematical and physical equations, accurate NWP requires an accurate initial state of the atmosphere and an accurate expression of the physical processes in the atmosphere (Bjerknes, 1904). Data assimilation (DA) is an effective technique for reducing uncertainties in the initial conditions (Talagrand, 1997), especially when advanced DA methods are used for targeted assimilation of the observations (Mu, 2013; Feng et al., 2022; Gao et al., 2022; Qin et al., 2023). In addition, the atmosphere has a chaotic nature (Lorenz, 1963), and NWP has unavoidable initial and model errors (Lorenz, 1969, 1995). Thus, compared to a “single-deterministic” forecast with large uncertainties, an ensemble-probabilistic forecast is a preferred way of reducing prediction uncertainty and improving prediction skill (Du and Chen, 2010; Mu et al., 2017). It can thus be concluded that targeted assimilation of observations to reduce the marine-BL wind error in the initial model fields, combined with an ensemble forecast, should contribute to improving the model’s predictive ability for

coastal warm-sector HR.

Some previous studies have used various DA methods to assimilate data from multiple sources to improve the model forecast skill for severe convective weather over southern China. For example, Bao and Yang (2015) used an ensemble Kalman filter (EnKF) method to assimilate the sounding observations; Bao et al. (2017) and Yue and Meng (2017) used an EnKF to assimilate the Doppler radar radial velocity. Zhang et al. (2016) and Gao et al. (2022) used the three-dimensional variational (3DVar) method to assimilate wind profiling radar observations and the ECMWF reanalysis version 5 (ERA5)-derived BL temperature. Pan et al. (2020) used the 3DVar system to assimilate Doppler radar radial velocity and a cloud analysis system to assimilate radar reflectivity, and Wu Y. L. et al. (2020) used the four-dimensional variational (4DVar) method to assimilate the Advanced Himawari Imager satellite radiance. Moreover, by using the analysis fields generated by ensemble-based DA as the initial ensemble fields, the convective-scale ensemble-probabilistic forecast has proven to be helpful in issuing early severe weather warnings in recent years (Roeber et al., 2004; Stensrud et al., 2009, 2013; Yussouf et al., 2013, 2015; Karstens et al., 2015; Zhang and Zhang, 2018). However, few studies have discussed how to effectively assimilate radar data to improve the probability prediction of warm-sector HR in coastal southern China.

In this study, on the basis of understanding the critical factors influencing the evolution of convection and the resultant rainfall, targeted assimilation of observations is conducted to improve the forecast skill: this is defined as “targeted assimilation.” As previously mentioned, the marine-BL airflow is a critical factor influencing the warm-sector HR in coastal southern China. Therefore, operational weather radar data in coastal areas are good targets for assimilated data for the coastal HR events, because the coastal operational radar can provide high spatiotemporal resolution wind-field observations over parts of the offshore areas within its detection range, which fills in for the lack of marine observations. Some studies have noted that coastal radar radial-velocity assimilation positively improves landfalling typhoon rainfall predictions (Zhu et al., 2016; Yue and Meng, 2017).

A warm-sector HR event associated with a BLJ occurred on the west coast of Guangdong Province on 8 May 2013 (Bao et al., 2017, 2021). For this event, previous studies found that the intensity of the marine-BL easterly airflow played a key role in determining the time and location of convective initiation (Bao et al., 2021), and the cyclic radar velocity data assimilation (VrDA)

during the early stage of this HR event could indeed improve the probability forecast of the convection evolution in this case (Bao et al., 2017). However, some issues still require further investigation: (1) What are the characteristics of the forecast error in experiments without DA and how are they formed? (2) What are the changes in the initial ensemble fields through VrDA, and how do these changes improve the ensemble probability forecast?

The remainder of this paper is organized as follows. Section 2 presents an overview of the case. The experimental designs of the radar velocity data assimilation (RadarDA) and no data assimilation (NODA) simulations are introduced in Section 3. Section 4 demonstrates the performance of the ensemble experiments. How the VrDA could improve the probabilistic forecast skill is discussed in Section 5. Finally, Section 6 provides a summary and conclusions.

2. Overview of the case

In this case, convective cells generated near Yangjiang City at about 0200 LT (local time = UTC + 8 h) 8 May 2013 and then grew quickly and expanded north-eastward to form a band-shaped and northeast–southwest-oriented mesoscale convective system (MCS; Figs. 1a₁–a₅). The HR (> 100 mm) mostly occurred in the lowlands southeast of the coastal mountains (Bao et al., 2021), while the maximum 8-h (0400–1200 LT 8 May) accumulated rainfall was more than 300 mm and located in central Yangjiang City (Fig. 2a).

Two sets of 60-member ensemble experiments without (NODA) and with radar velocity DA (RadarDA) were conducted for this event (Bao et al., 2017) based on WRF Version 3.5.1 (Skamarock et al., 2008) and the WRF-based EnKF system that was developed by the Pennsylvania State University (Zhang et al., 2006, 2009; Meng and Zhang, 2007, 2008a, b). The WRF has the necessary skills for providing a high-level single-deterministic forecast [the optimal experiment (OPT)] for this coastal HR event (Bao et al., 2021). Specifically, among the 60-member NODA, the one member (mem29) producing the most accurate convection at the time and location of initiation and with the highest forecast skill for convection evolution was selected as the OPT. The OPT could reproduce this HR event and accurately capture the convection evolution (Figs. 1b₁–b₅, 2b). However, the NODA has a low forecast probability for the convection evolution. Similar to that used in Bao et al. (2017), the

neighborhood ensemble probability (NEP) method (Schwartz et al., 2010) is used to verify the probability forecast of convection evolution. Figures 1c₁–c₅ show the NEP of NODA that predicted the radar composite reflectivity exceeding 15 dBZ during 0400–1200 LT. The NEP values of NODA are less than 0.6, and the high-NEP areas are much smaller than the observed MCS regions throughout the forecast stage. Low ensemble-forecast skill indicates that this case may have low practical predictability.

3. Experimental design

In the two sets of ensemble experiments (NODA and RadarDA), three one-way-nested domains (D1–D3) are utilized with respective grid resolutions of 27, 9, and 3 km. There are 43 vertical levels, and the model top is at 10 hPa. The innermost domain (D3) covers southern China and the adjacent oceans (Fig. 3a). The NODA ensemble experiment initiates at 2000 LT 7 May 2013, and the initial states of its 60 members are generated by adding balanced perturbations to the NCEP final operational global (FNL) analysis at the initial time. The perturbations are generated by using the “cv3” background error covariance option in the WRF 3DVar package (Barker et al., 2004). The domain-averaged standard deviations of the perturbed variables are approximately 2 m s⁻¹ for horizontal winds, 1 K for temperature, and 0.5 g kg⁻¹ for the water-vapor mixing ratio. The RadarDA ensemble experiment is performed with the same perturbed ensemble initial fields as NODA has, and it is first integrated for 6 h to develop a flow-dependent background error covariance structure before assimilation. Many studies have verified that 6 h is sufficient time to develop a flow-dependent background error covariance with an initial coarse-resolution global analysis (e.g., Qiu and Zhang, 2016; Bao et al., 2017; Yue and Meng, 2017). The DA starts at 0200 LT 8 May with a 6-min interval and 2-h span. Then, the RadarDA ensemble forecasts are initiated from the EnKF analysis fields of 60 ensemble members at the DA end time (0400 LT). All these experiments are integrated up to 1200 LT 8 May (Fig. 3b). NODA and RadarDA utilize the same physical parameterization schemes as Bao et al. (2017, 2021) do, namely the WRF Single-Moment 6-class microphysics scheme (WSM6; Hong et al., 2004), the Yonsei University (YSU) PBL scheme (Noh et al., 2003), the thermal-diffusion land-surface scheme (Chen and Dudhia, 2001), the Rapid Radiative Transfer Model longwave radiation

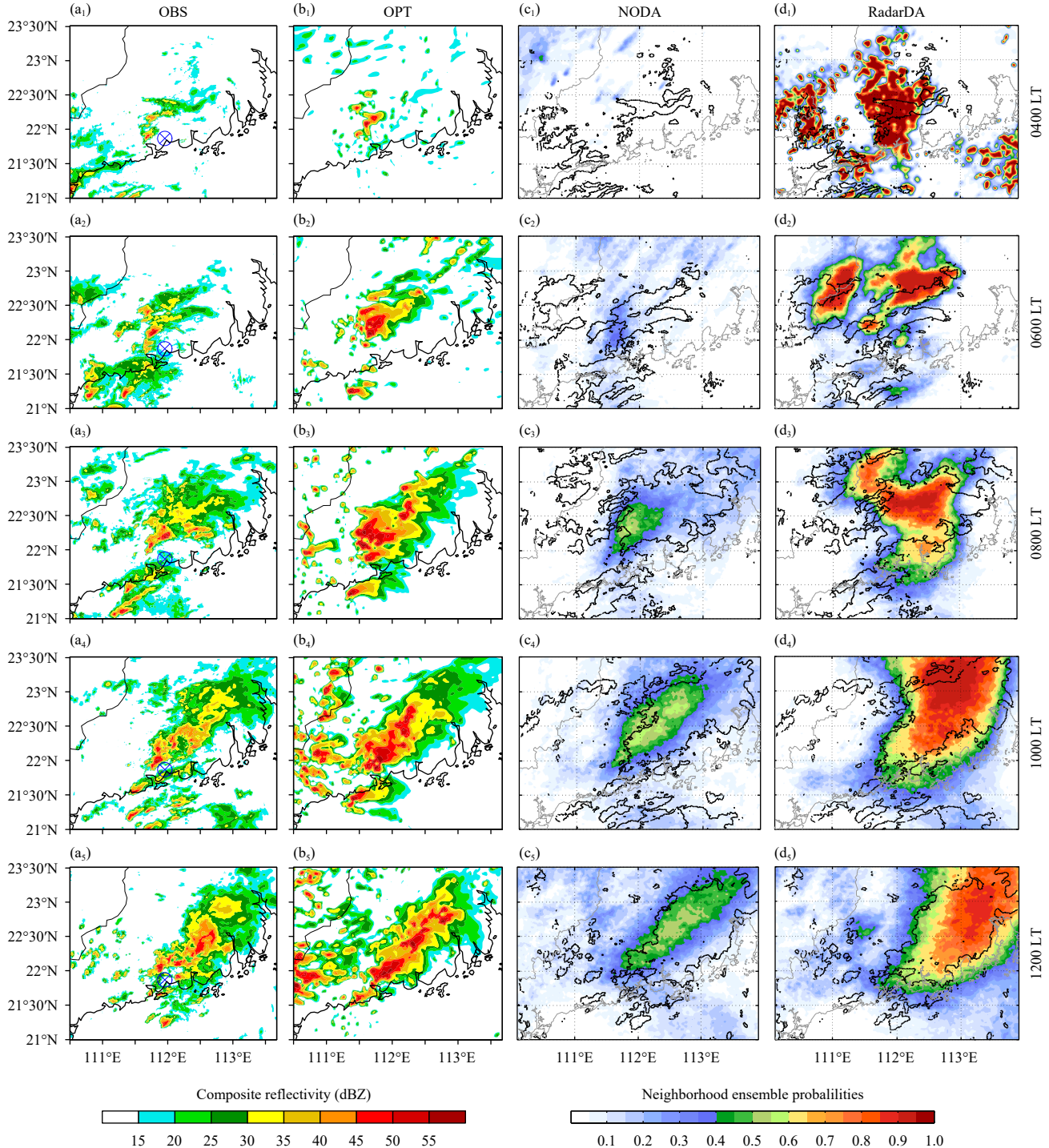


Fig. 1. Radar composite reflectivity (dBZ) derived from (a₁–a₅) the Yangjiang radar (OBS) and (b₁–b₅) the optimal experiment (OPT). The neighborhood ensemble probabilities (NEP; shaded) of (c₁–c₅) NODA and (d₁–d₅) RadarDA that predicted the radar composite reflectivity exceeding 15 dBZ every 2 hours during 0400–1200 LT 8 May 2013. The regions of radar composite reflectivity exceeding 15 dBZ observed by the Yangjiang radar at the corresponding times are outlined by bold black lines in (c₁–c₅) and (d₁–d₅). The blue crossed circles in (a₁–a₅) denote the location of the Yangjiang radar.

scheme (Mlawer et al., 1997), and the Dudhia (1989) shortwave radiation scheme. The Grell–Freitas ensemble cumulus scheme (Grell and Freitas, 2014) is turned on in D1 and D2, whereas no cumulus parameterization is used

in D3.

The assimilated radar velocity data are from the Yangjiang operational S-band Doppler radar located on the coast of Guangdong Province. For the raw radar velo-

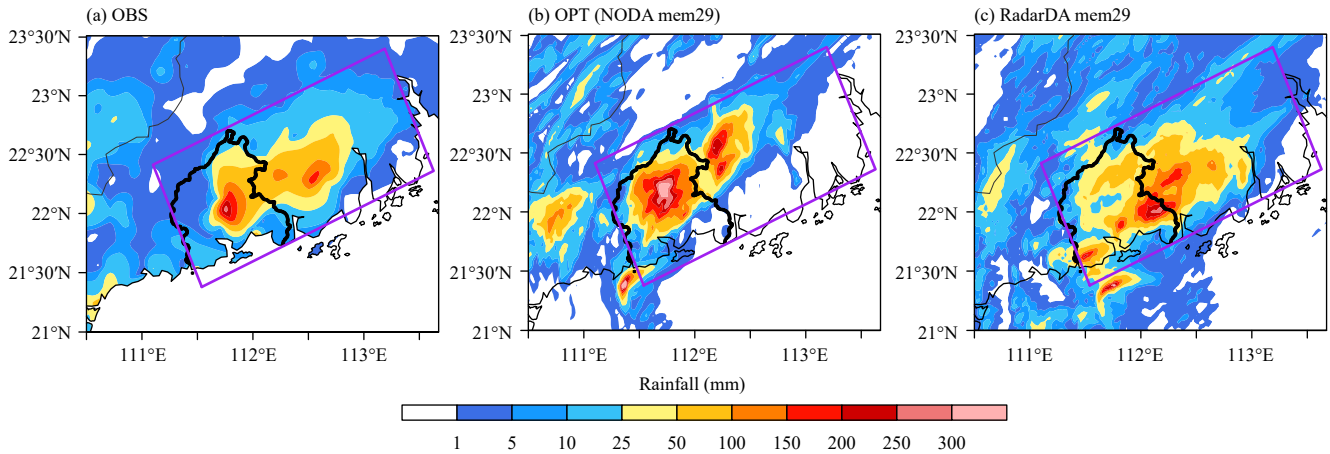


Fig. 2. Rainfall accumulation during 0400–1200 LT 8 May 2013 from the (a) rain-gauge observations, (b) OPT (NODA mem29) experiments, and (c) RadarDA mem29 experiments. The bolded black curves represent the boundary of Yangjiang City. The purple rectangles denote the key region of this study.

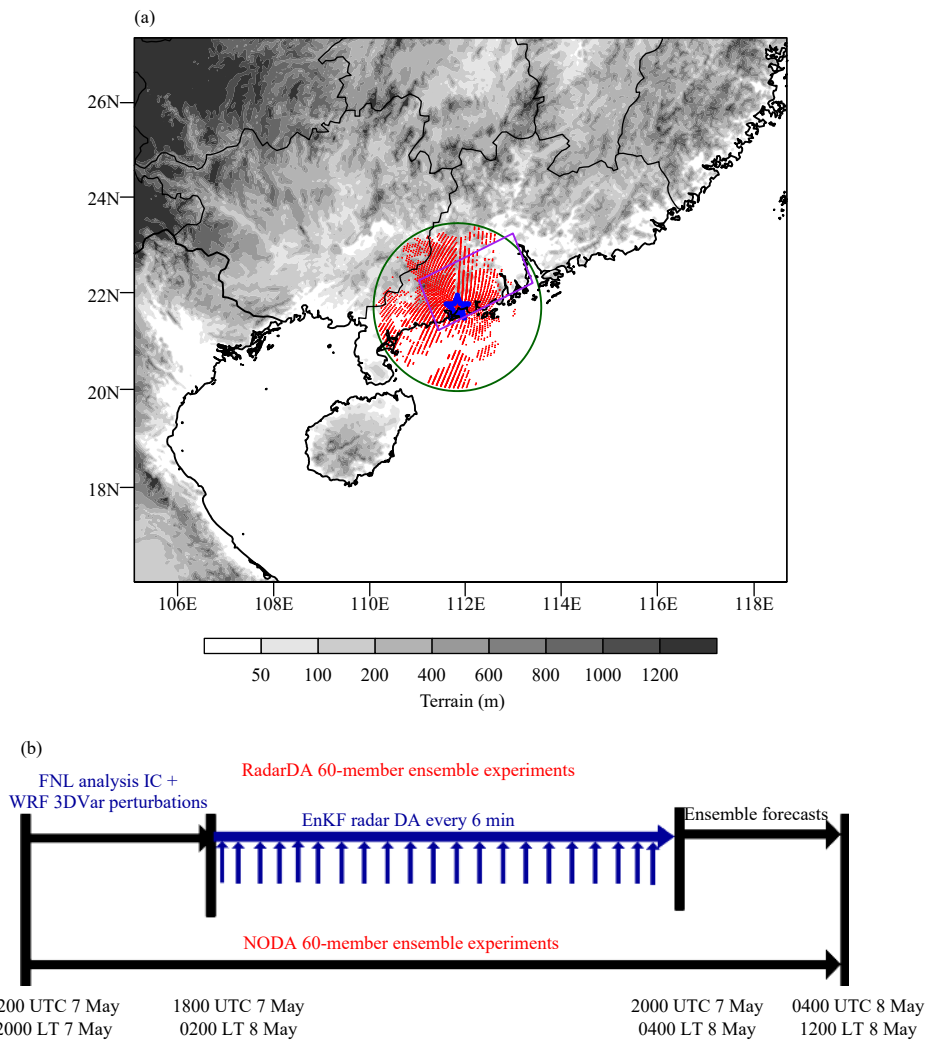


Fig. 3. (a) Plot of terrain elevations (gray shadings; m) in D3. Location of the Yangjiang radar is marked by a blue star. Red dots show the distribution of super observations (SOs) at 0200 LT 8 May 2013. The purple box over coastal southern China denotes the key region. The dark green circle marks the area with a radius of 200 km centered at the Yangjiang radar. (b) Schematic flowcharts for the RadarDA and NODA 60-member ensemble experiments.

city data, the quality control and data thinning methods proposed by Zhang et al. (2009) are used to produce the “super” observations (SOs; Fig. 3a). The SOs are assimilated into the WRF-based EnKF system. The experimental design of the RadarDA is similar to that of the EXP37 in Bao et al. (2017). Therefore, please refer to Bao et al. (2017) for more details on the assimilation scheme.

4. Impact of RadarDA on ensemble forecasts of convection evolution and the resultant rainfall

The NEP method (Schwartz et al., 2010) is used to verify the probability forecast of convection evolution. Figures 1c₁–1c₅ and 1d₁–1d₅ show the NEP of the radar composite reflectivity (dBZ) that exceeds 15 dBZ in NODA and RadarDA during 0400–1200 LT 8 May 2013. The VrDA can remarkably improve the probability forecast skill on the evolution of an HR-producing MCS during the convection initiation and development stages. Before DA, NODA has a very low probability of convection evolution, and the high-NEP area is smaller than that of the observed MCS throughout the forecast period. NEP values are below 0.3 in the early stages (before 0600 LT) and then increase but remain smaller than 0.6 (Figs. 1c₁–c₅). After DA, the NEP values near the observed MCS are up to 0.8–1, although with some displacement errors before 0800 LT (Figs. 1d₁–d₅). Note that the high-NEP areas at 0400 LT are much larger than the observed convection regions (Fig. 1d₁), due to the rapid multi-cycle assimilation with a 6-min time interval and 2-h time span resulting in convection in each member occurring at/around the correct regions but with stronger intensities and larger domains at the initial time after DA. The best probability forecast of RadarDA is at the convection maturity stage. During 1000–1200 LT, the large NEP value (> 0.6) area nearly coincides with that in the observations (Figs. 1d₄, d₅). The mean NEP averaged over the regions of the HR-producing MCS during 1000–1200 LT has a big increase from 0.33 in NODA to 0.68 in RadarDA. Generally, RadarDA can forecast the convection evolution better than NODA can, with more accurate times, locations, scopes, and moving speeds.

The improvement in the ensemble-forecast performance comes from improvement of the deterministic forecast skill of most members. To quantitatively compare the forecast skill between the NODA and RadarDA ensemble members for the MCS evolution, the 9-h (0400–1200 LT) sum area under the relative operating characteristic (ROC) curve (AUC; Mason and Graham, 1999, 2002; Bao et al., 2017) with a radar composite reflectiv-

ity value greater than 15 dBZ over the region shown in Fig. 1 is calculated (Fig. 4). A higher score indicates better forecast skill. Mem29 has the highest score among the 60-member NODA, indicating that it has the best forecast skill for the MCS evolution; this is one of the main selection criterion for the OPT. The comparison results show that the forecast skill of 95% of the members (57/60) increases by 0.6%–37.6% after VrDA, which reflects the high efficiency of VrDA in improving the ensemble forecast of convection evolution.

To measure the HR forecast skill of all the ensemble members quantitatively, the fractions skill score (FSS; Roberts and Lean, 2008; Luo and Chen, 2015; Bao et al., 2021) is applied to an 8-h accumulated rainfall amount of 50 mm with a 15-km neighborhood size for each member of NODA and RadarDA. The FSS value (0.3) of the FNL experiment in Bao et al. (2021) (a deterministic experiment with the initial field provided by NCEP FNL) and the observed area-averaged precipitation (31.5 mm) over the key region (marked by the purple rectangle in Fig. 2a) are used as two reference values to estimate the rainfall forecast skill of these members (Fig. 5a). The mean FSS of the 60 members shows significant improvement from 0.21 before DA to 0.44 after DA. As can be seen, 44 (~75%) of the 60 NODA ensemble members have low forecast skill (FSS < 0.3), and 22 members forecast the area-averaged rainfall to be less than 9 mm (< 1/3 of the observed rainfall). After DA, the high-score (FSS > 0.3) members increase from 16 to 45, while the FSS values for 39 of the 44 low-score (FSS < 0.3) NODA members increases by 0.01–0.77. These 39 NODA members, which have FSS values less than 0.3 that then increase after DA, are defined as the “low-skill” NODA members. However, some RadarDA ensemble members forecast rainfall amounts greater than the observation amounts. There are 16, 11, and 3 members that

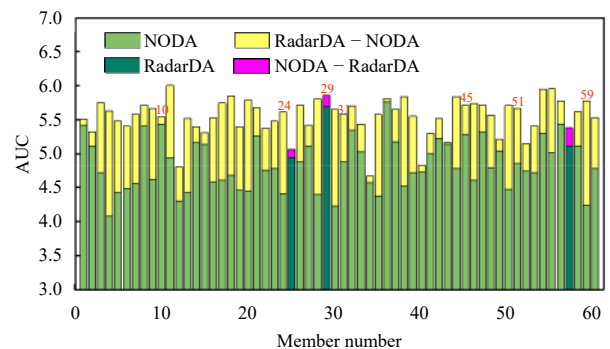


Fig. 4. The 9-h (0400–1200 LT) sum area under the ROC curve (AUC) with radar composite reflectivity values ≥ 15 dBZ from the NODA and RadarDA ensemble experiments. The red numbers mark ensemble members of particular interest.

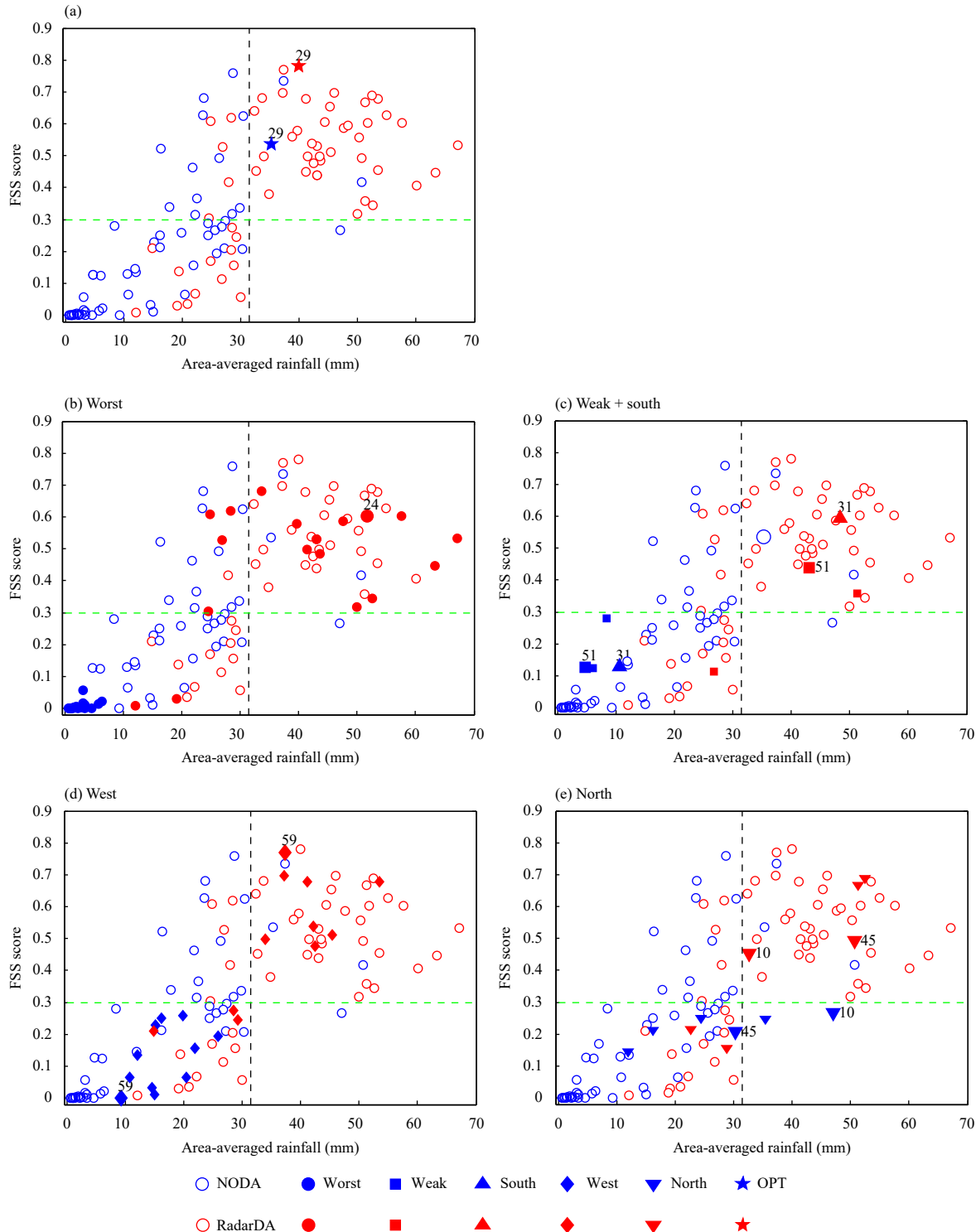


Fig. 5. Scatter plots of the 8-h rainfall accumulation (mm) averaged over the key region (the purple rectangle in Fig. 2a) versus the FSS for the 8-h rainfall accumulation exceeding 50 mm for (a) NODA and RadarDA, and the defined sub-groups of the NODA and corresponding RadarDA ensemble experiments: (b) worst, (c) weak + south, (d) west, and (e) north. The classification of sub-groups is summarized in Table 1 and discussed in the main text. The dashed black line represents the observed area-averaged rainfall of 31.5 mm. The green line indicates the value of the FNL-simulated FSS of 0.3.

calculated 40–50, 50–60, and > 60 mm of area-averaged precipitation, respectively.

Overall, the low-skill NODA members either have large forecast errors in the rainfall amounts or large fore-

cast errors in the rainfall location. Therefore, to display the NODA forecast error characteristics, analyze the reasons for the error, and demonstrate and discuss why VrDA improves the ensemble-forecast skill, we divide the 39 low-skill NODA members into two main groups (Table 1). One group is named poor forecast of rainfall amount, and the members significantly underestimate rainfall amounts, with the 8-h area-averaged rainfall accumulation being less than 1/3 of the observation (< 9 mm). The other group is named poor forecast of rainfall location, and these members have better rainfall amount forecasts (the area-averaged 8-h rainfall accumulation > 9 mm) but large rainfall displacements. Considering the area-averaged rainfall amounts and FSS, the main poor forecast of rainfall amount group is further divided into two sub-groups, i.e., the worst group (with over-underestimated rainfall amounts and $\text{FSS} < 0.1$) and the weak group (with underestimated rainfall amounts and a mid-level FSS). Considering the rainfall location relative to the symmetry axes of the key region, the main poor forecast of rainfall location group is further divided into three sub-groups, i.e., the south (north) group with most of the HR (> 25 mm) in the region mainly to the south (north) of the northeast–southwest symmetry axis, and the west group with most of the HR in the region to the west of the northwest–southeast symmetry axis (Table 1, Figs. 5b–e, 6). For 39 low-skill members, 38 members among them are divided into these 5 sub-groups, while the remaining one member (mem37) is not classified into any sub-groups since it has the best forecast skill ($\text{FSS} = 0.28$; area-averaged rainfall = 26.8 mm). To more clearly show the forecast error characteristics of the five sub-groups, we selected a representative member from each sub-group as follows: mem24 (worst), mem51 (weak), mem31 (south), mem59 (west), and mem45 (north) (Table 1, Figs. 6a₁–e₁).

The comparison of the sub-groups and their representative members between NODA and RadarDA demonstrates that VrDA can reduce the forecast error in the

rainfall intensity and location in both main groups of “poor forecast of rainfall amount” and “poor forecast of rainfall location” (Fig. 6); they can also reduce the forecast error of convection evolution, including the time, location, morphology, and moving speed (Figs. 7, 8). The accumulated rainfall amounts of mem24 and mem51 in RadarDA increase sharply, but they are significantly underestimated in NODA (Figs. 6a₁, a₂, b₁, b₂). The rainfall locations of mem31, mem59, and mem45 in RadarDA are adjusted to be more accurate, moving them to the north, southeast, and south in NODA, respectively. The five representative members in RadarDA forecast the rainfall amounts and locations much better, and thus have larger FSS values (Figs. 5b–e, 6a₁–e₁, a₂–e₂). In addition, the average accumulated rainfall of these sub-groups in RadarDA is close to that of the observations, although they have weaker intensities (Figs. 6a₃–e₃, a₄–e₄). The radar composite reflectivity from the five representative members of NODA (Fig. 7) demonstrate that convection occurs later and/or develops weaker results with underestimated rainfall amounts, and convection that occurs at incorrect locations induces rainfall that occurs in the wrong area. Specifically, VrDA can encourage the convection to initiate earlier in the delayed-convective-initiation NODA members (mem24, mem51, mem31, and mem 59), or it can adjust convection to occur and develop closer to the correct position in NODA members at the wrong locations (mem31, mem59, and mem45). Therefore, the convection evolution in RadarDA members is more consistent with that in the observations, and more accurate convection evolution makes the rainfall intensity and location more similar to the intensity and location of the observations.

The forecast skill levels of the “poor forecast of rainfall amount” group and the “poor forecast of rainfall location” group are improved through VrDA. VrDA also has a positive effect on the forecast of the OPT experiment overall. The rainfall location is adjusted southward (Figs. 2b vs. 2c), and the FSS increases from 0.54 to

Table 1. Classification of the NODA ensemble members with low forecast skill ($\text{FSS} < 0.3$)

Main group	Criterion	Sub-group	Criterion	Number of members	Representative member
Poor forecast of the rainfall amount	Significant underestimation of the rainfall amount, with the area-averaged 8-h rainfall accumulation < 9 mm	Worst	The lowest FSS (< 0.1) and the least amount of rainfall	18	24
		Weak	The mid-level FSS, i.e., $0.1 < \text{FSS} < 0.3$	3	51
Poor forecast of the rainfall location	The area-averaged 8-h rainfall accumulation > 9 mm but with large rainfall displacement	South	The rainfall is displaced more to the south	1	31
		West	The rainfall is displaced more to the west	11	59
		North	The rainfall is displaced more to the north	5	45

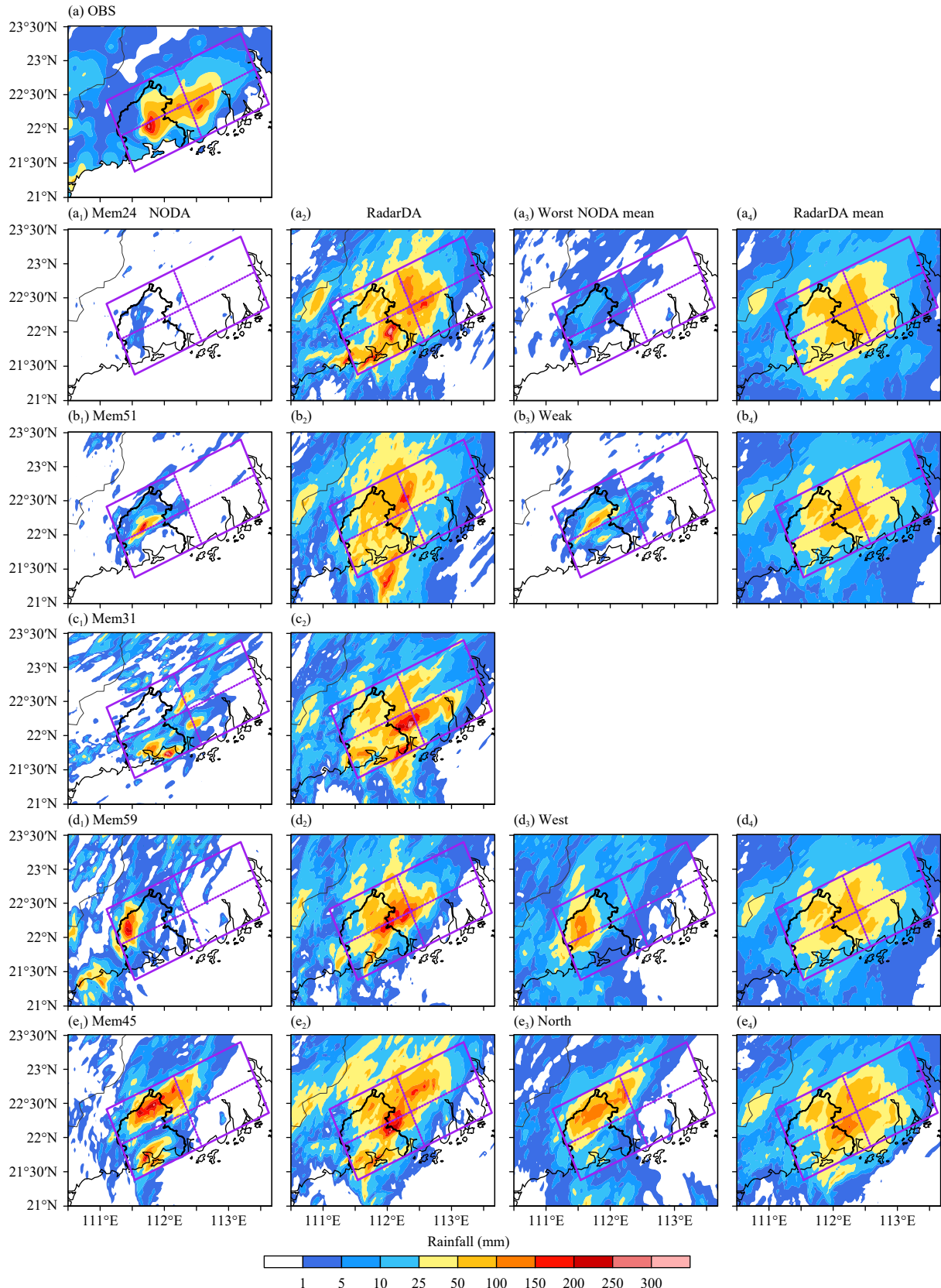


Fig. 6. Comparisons of the rainfall accumulation of the (a) observations, five representative members in (a₁–e₁) NODA and (a₂–e₂) RadarDA, as well as the average of the four sub-groups of (a₃–e₃) NODA and (a₄–e₄) RadarDA during 0400–1200 LT 8 May 2013. The two purple dotted lines are the symmetry axes of the key study region.

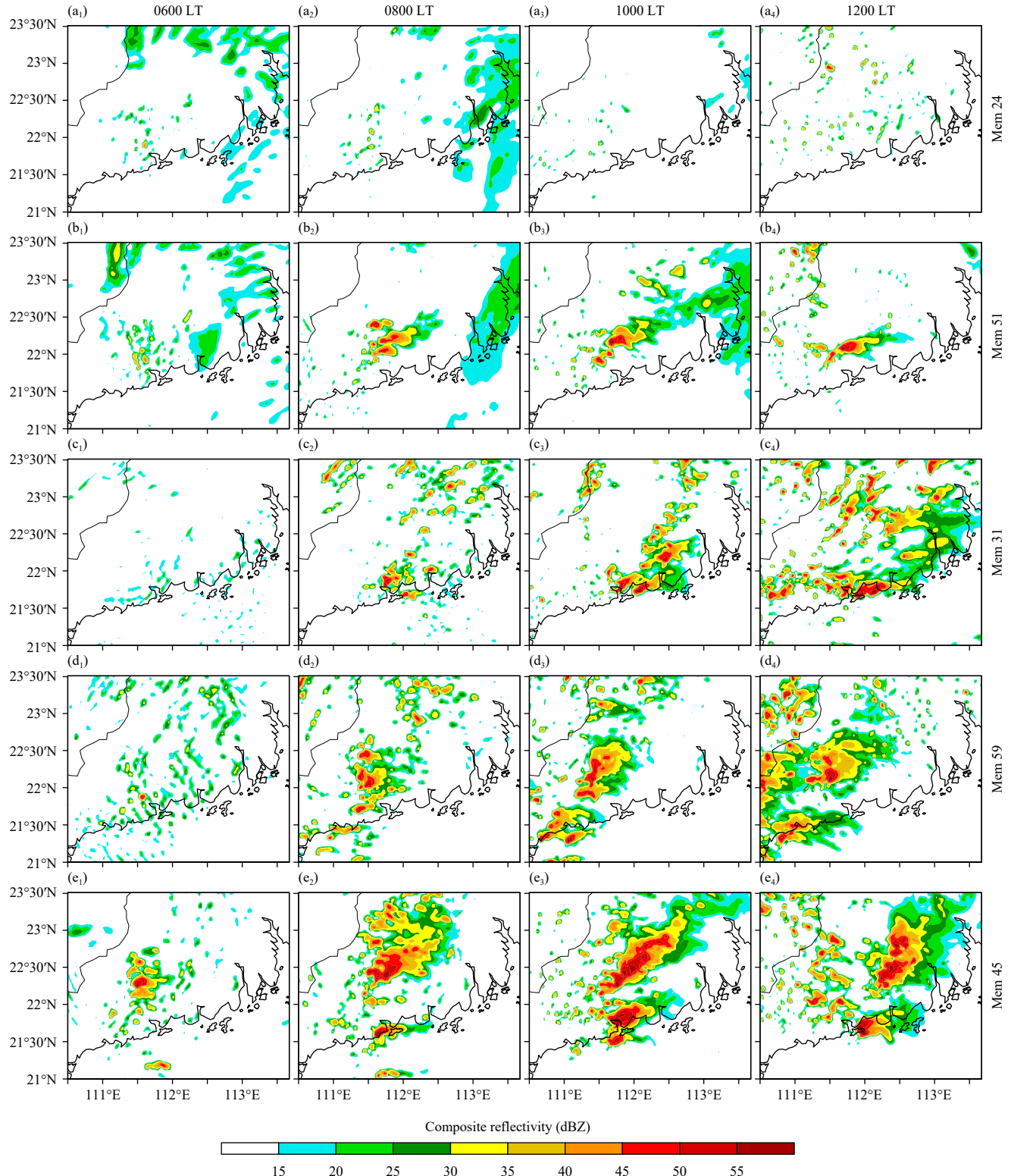


Fig. 7. Radar composite reflectivity (dBZ) from the five representative members of NODA listed in Table 1 every 2 hours during 0600–1200 LT 8 May 2013.

0.78. However, the 9-h sum of the AUC slightly decreased by about 2% (Fig. 4); this may be because the RadarDA mem29 forecasts a larger convective system at

the west of HR-producing MCS than OBS in the early stages (around 0600 LT, figure omitted), as the five representative members do (Figs. 8a₁–e₁), but OPT fails to

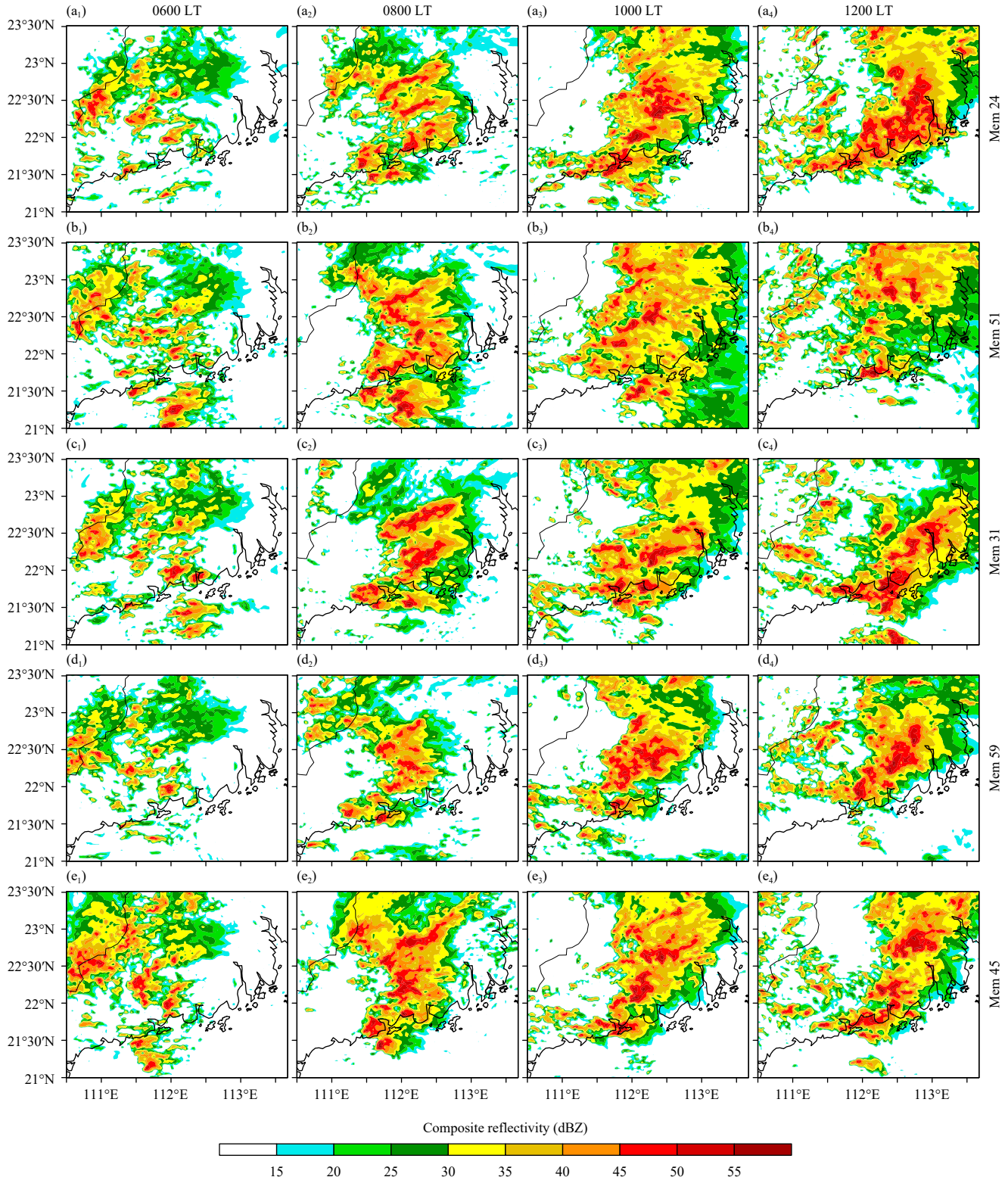


Fig. 8. As in Fig. 7, but for RadarDA.

forecast it (Fig. 1b₂).

In summary, VrDA can improve the deterministic forecast skill of convection evolution in most members, and the more realistic convection evolution forecast then

results in a much better forecast of rainfall intensity and location. The improvement in the deterministic forecast of most members further leads to improved performance of the ensemble-probabilistic forecast.

5. How can assimilating radar data improve the ensemble forecast

Accurate rainfall forecasts are closely related to accurate forecasts of moisture transport (Yue and Meng, 2017). Bao et al. (2021) have demonstrated that the marine-BL southeasterly airflow is the crucial factor influencing convection initiation and the resultant rainfall accumulation, while the moisture field has relatively less impact on this particular HR event that occurred in coastal southern China with rich water-vapor fields. Thus, the BL environmental wind fields at the initial RadarDA time (0400 LT, i.e., the end time of DA) and the evolution of moisture transport during the entire RadarDA 8-h forecast period (0400–1200 LT) are compared between the NODA and RadarDA members to determine the physical reasons for the forecast error and why assimilating radar data can improve the ensemble-forecast skill. In this comparison, the OPT is used as the benchmark for evaluation due to its excellent ability to forecast the rainfall and convection evolution for this case.

In the OPT, a strong marine southeasterly BLJ (wind speed $> 12 \text{ m s}^{-1}$; Figs. 9a, c) from the northern South China Sea transports moist air to coastal southern China and produces horizontal convergence and upward lifting when encountering the coastal terrain. This situation is favorable for the occurrence of HR on the lowlands southeast of the mountains in coastal southern China (Bao et al., 2021). Referring to Yue and Meng (2017), the evolution of the upstream low-level southeasterly moisture transport towards coastal southern China in

OPT during 0400–1200 LT was then examined (Fig. 9b). It is evident that there is a persistent inflow of moisture exceeding $375 \text{ kg m}^{-1} \text{ s}^{-1}$ into the key region through the southeast boundary roughly between 111.5° and 113.7°E from 0500 LT, and through the entire boundary about 2 h later, indicating enhancement of the moisture supply. This evolution of moisture transport corresponds well with the convection development and rainfall evolution. Compared to the OPT, the composite marine-BL wind field of the poor forecast of rainfall amount group is much weaker, with wind speeds $< 10 \text{ m s}^{-1}$ (Figs. 10a, 11a). Conversely, the poor forecast of rainfall location group (excluding the south sub-group) has the stronger marine-BL airflow with the wind speed mainly ranging between 11.5 and 13.5 m s^{-1} (Figs. 10c, 11b). This illustrates the high correlation between the intensity of the BL airflow and rainfall amounts. Stronger low-level airflow facilitates stronger water-vapor transport. Note that the south sub-group is an exception in the poor forecast of rainfall location group, in that it does not have a stronger BLJ intensity (Fig. 12c₁). Thus, the south sub-group is excluded from the analysis here.

A further comparison of the BL wind field and the evolution of low-level moisture transport between the five representative members and OPT is carried out, and then, we analyze the reasons for the forecast errors for convection evolution and rainfall intensity and location in detail. For mem24 (worst), mem51 (weak), and mem31 (south), the marine-BL airflows are weaker than the southeasterly wind (mostly smaller than 10 m s^{-1}). Accordingly, the low-level moisture transport in these

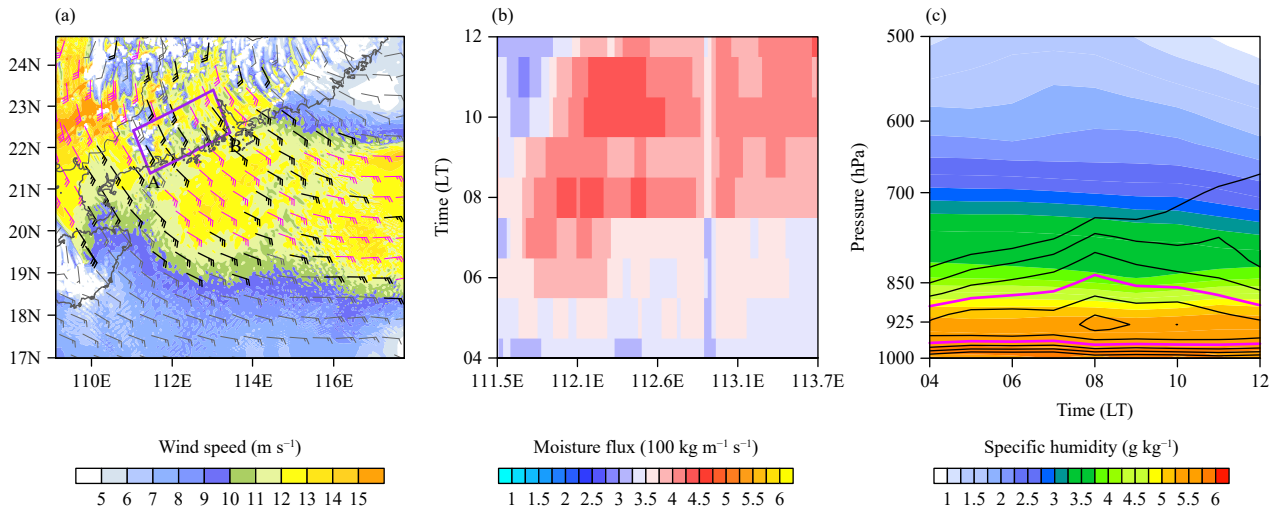


Fig. 9. Results from the OPT experiment: (a) 950-hPa wind (full barb = 5 m s^{-1} , magenta = $> 12 \text{ m s}^{-1}$, black = $10\text{--}12 \text{ m s}^{-1}$, and gray = $< 10 \text{ m s}^{-1}$) and wind speed (shaded; m s^{-1}) at 0400 LT; (b) time-longitude plot of the vertically integrated (from the surface to 700 hPa) moisture flux ($100 \text{ kg m}^{-1} \text{ s}^{-1}$) across line AB in (a); and (c) pressure-time plot of the averaged specific humidity (shaded; g kg^{-1}) and wind speed (contours; $> 6 \text{ m s}^{-1}$, magenta = 10 m s^{-1}) across line AB during 0400–1200 LT 8 May 2013.

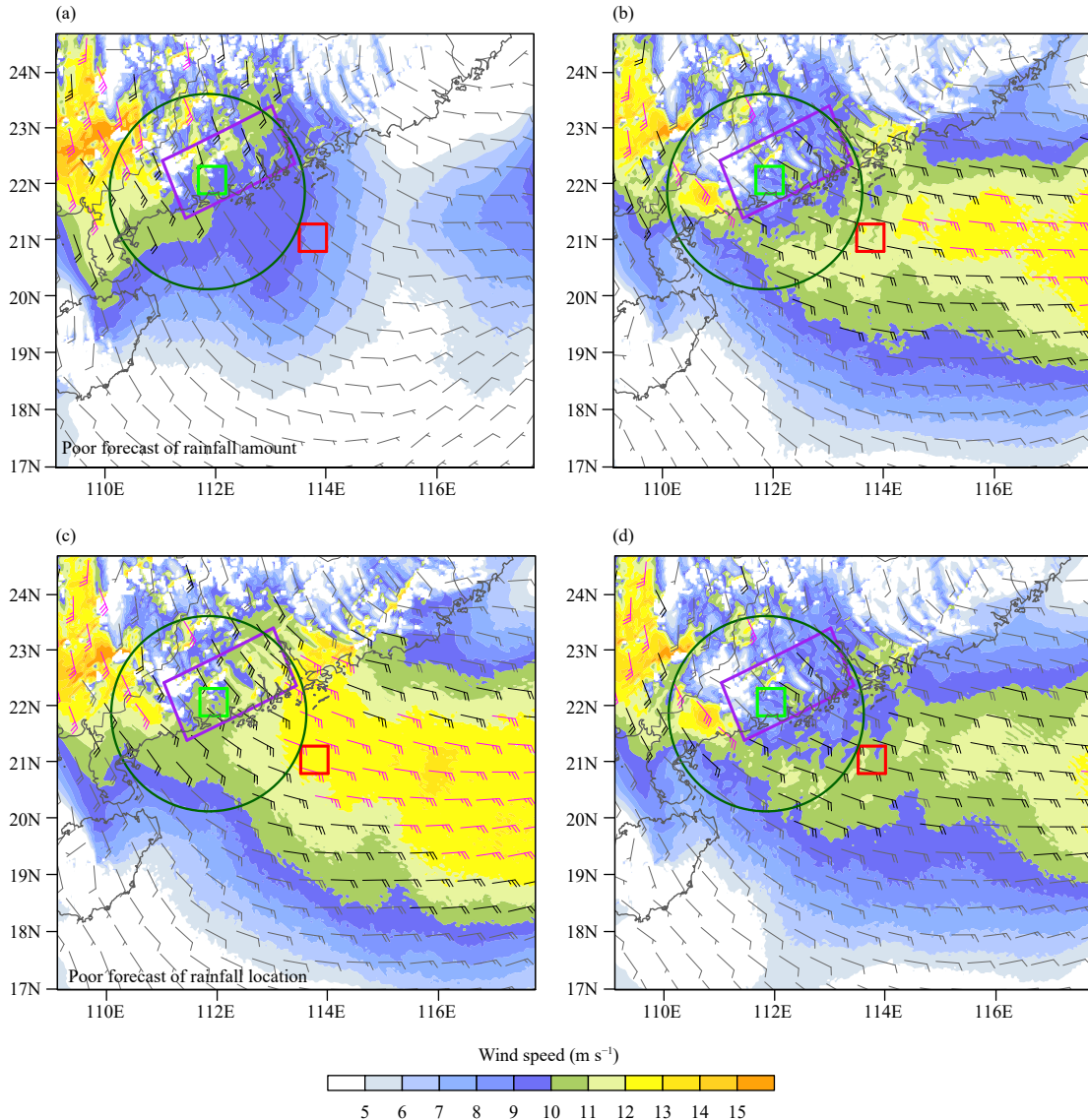


Fig. 10. Comparisons between (a, c) the group of low-forecast-skill members from NODA and (b, d) the corresponding members from RadarDA: composite 950-hPa wind field (full barb = 5 m s^{-1} , magenta $> 12 \text{ m s}^{-1}$, black = $10\text{--}12 \text{ m s}^{-1}$, and gray $< 10 \text{ m s}^{-1}$) and wind speed (m s^{-1}) at 0400 LT. (a, b) The poor forecast of rainfall amount group and (c, d) the poor forecast of rainfall location group (excluding the south sub-group). The purple box indicates the key region, the green box indicates the coastal convection area, the red box indicates the offshore upstream area, and the dark green circle marks the area with a radius of 200 km centered at the Yangjiang radar.

members is also weaker than that in OPT ($< 350 \text{ kg m}^{-2} \text{ s}^{-1}$) over the 8-h forecast period. The weaker BL airflows and weaker moisture transport (Figs. 12a₁–c₁) cause the convection to occur later and/or too far south, and its subsequent development is weaker (Figs. 7a₁–a₄, b₁–b₄, c₁–c₄). This result leads to less rainfall or to a more southerly rainfall location (Figs. 6a₁–c₁). For mem59 (west), the BL airflows have stronger easterly components (Fig. 12d₁), which encourage the moisture to be transported to a more westerly position (Fig. 13d₁). Thus, convection and rainfall happen in areas farther west than in the observations (Figs. 6d₁, 7d₁–d₄). For mem45 (north), compared to the OPT, the BL airflows

are similar in direction but are larger in speed (Fig. 12e₁). The stronger southeasterly BL airflow induces stronger moisture transport (Fig. 13e₁), more severe convection, and heavier rainfall to the north of the observed rain belt (Figs. 6e₁, 7e₁–e₄). Generally, the comparison results confirm that the convection initiation time and location, convection intensity and morphology, and rainfall intensity and location significantly correlate with the intensity and direction of the marine-BL airflow and the moisture transport. The errors in the intensity and direction of the BL wind field and related low-level moisture transport are the main reasons for the forecast errors for the rainfall and convection evolution.

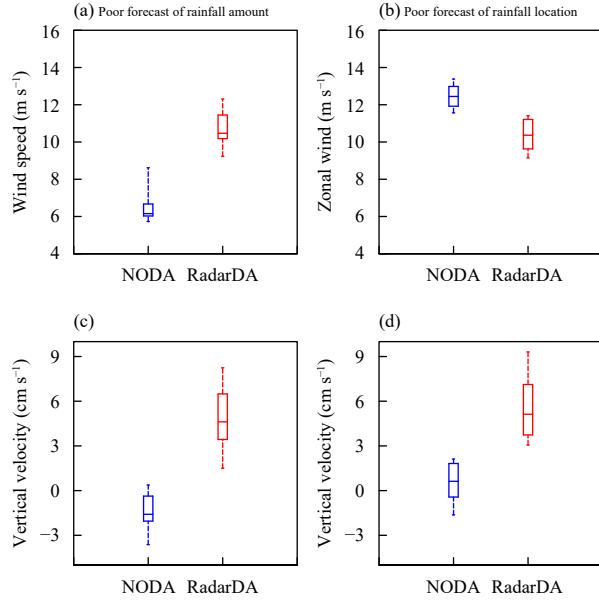


Fig. 11. Box-and-whisker plots of (a, b) the regionally averaged 950-hPa wind speeds over the offshore upstream area (marked by the red box in Fig. 10) and (c, d) the regionally averaged 700-hPa vertical velocities over the coastal convection area (marked by the green box in Fig. 10) from the (a, c) poor forecast of rainfall amount group and (b, d) poor forecast of rainfall location group (excluding the south subgroup) of NODA and RadarDA.

VrDA directly reduced the initial wind-field error of the low-skill ensemble members (Fig. 10). After VrDA, the differences in intensity and direction between the composite BL wind of two low-skill groups and the BL wind of OPT are diminished to various degrees. In particular, the weaker (stronger) composite BL wind field of the poor forecast of rainfall amount (poor forecast of rainfall location) group becomes stronger (weaker) from NODA to RadarDA (Figs. 10, 11). Bao et al. (2021) calculated the backward trajectories in the BL in the OPT from 2000 LT 7 May (the initial time of the simulations) to 0200 LT 8 May (the oncoming time of convection initiation), and the starting calculation area was selected at the area of convection initiation. In this study, we chose two areas of $30 \text{ km} \times 30 \text{ km}$ located at the start and end areas of the backward trajectories, respectively, from coastal southern China and its adjacent sea as the representative HR area (small green box in Fig. 10) and the representative upstream area (small red box in Fig. 10), to compare the wind speed of marine-BL airflows and the vertical velocity over the coastal HR area between the NODA and RadarDA members from the two low-skill groups (Fig. 10). For the poor forecast of rainfall amount group, the wind speed of the marine-BL airflows changes from weak ($< 9 \text{ m s}^{-1}$) in NODA to strong in RadarDA (Fig. 11a). In contrast, for the poor forecast of rainfall

location group, the wind speed of the marine-BL airflows changes from strong (about $11\text{--}13.5 \text{ m s}^{-1}$) in NODA to weak in RadarDA (Fig. 11b). The median value of the wind speed in both groups is adjusted to around 10.5 m s^{-1} in RadarDA (Figs. 11a, b). The comparison of the BL wind fields between NODA and RadarDA of the five representative members also demonstrates the ability of VrDA to reduce errors in the marine-BL wind speed and direction in detail (Fig. 12). From NODA to RadarDA, the weaker BL airflows in mem24, mem51, and mem31 become stronger, the easterly wind in mem59 is adjusted to a southeasterly wind, and the stronger BL airflow in mem45 becomes weaker. As a result, the BL wind fields of these representative members become close to those of OPT. Moreover, the vertical motion at the middle level of the troposphere over the key region changes from a weak downdraft in the poor forecast of rainfall amount group or a weakly strong updraft in the poor forecast of rainfall location group in NODA to a strong updraft in RadarDA. The vertical velocities of most members in the two groups are adjusted to $3\text{--}7 \text{ cm s}^{-1}$ in RadarDA (Figs. 11c, d). The adjustments for the initial wind fields of these low-skill members to various degrees cause the convection to occur and develop at more accurate times and locations (Fig. 8).

The adjustments in the initial wind fields (at 0400 LT) lead to sharp changes in the marine low-level southeasterly airflows toward the critical region in the ensuing 8-h forecast period (0400–1200 LT; Figs. 13a₃–e₃). Specifically, for mem24, mem51, and mem31, VrDA mainly brings out positive increment with various degrees of low-level southeasterly airflows across the southeastern boundary of the key region during the entire forecast period (Figs. 13a₃–c₃). The positive increments in mem24 and mem51 peak around 925 hPa after 0600 LT with a maximum of up to 9 m s^{-1} , while the maximum increment in mem31 is about 7 m s^{-1} , which appears between 700 and 800 hPa after 0700 LT. For mem59, the southeasterly wind increments are generally positive values (up to 4 m s^{-1} below 650 hPa), but they turn from weakly negative to positive around 0800 LT below 900 hPa (Fig. 13d₃). For mem45, the southeasterly wind increments are mostly negative at low levels (below 700 hPa), with a maximum value of about -4 m s^{-1} (Fig. 13e₃), which favors a southward adjustment of the rainfall area. Besides the adjustment in wind fields, VrDA also affects the evolution of moisture fields (Figs. 13a₄–e₄), relying on the “flow-dependent” background error covariance used in the EnKF (Zhang and Snyder, 2007). Mem24 and mem45 have overall positive and negative low-level moisture increment, respectively,

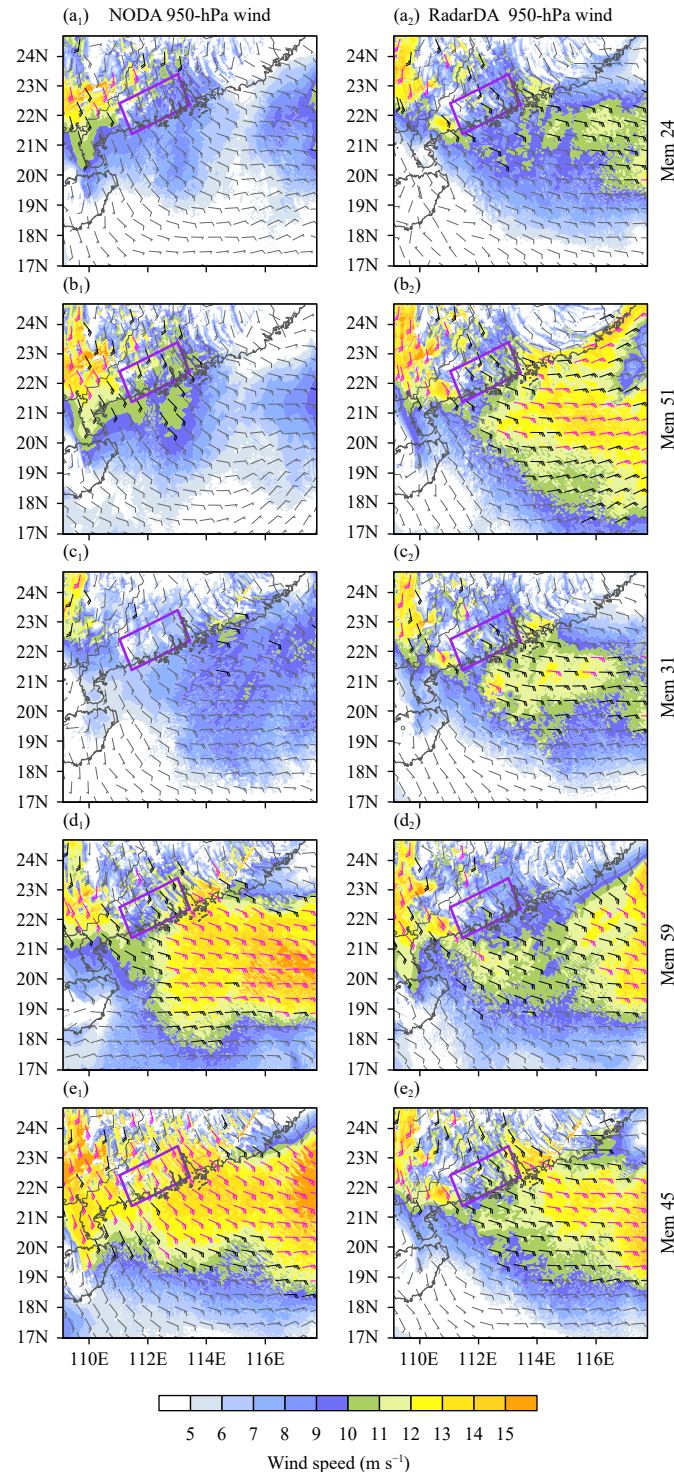


Fig. 12. Comparisons between (a₁–e₁) the selected five NODA representative members and (a₂–e₂) the corresponding RadarDA members of the 950-hPa wind field (full barb = 5 m s^{-1} , magenta $> 12 \text{ m s}^{-1}$, black = $10\text{--}12 \text{ m s}^{-1}$, and gray $< 10 \text{ m s}^{-1}$) and wind speed (shaded; m s^{-1}).

while the low-level moisture increments of mem51, mem31, and mem59 have alternating positive and negative features (Figs. 13b₄–d₄). Overall, the moisture increments in these five representative members vary in a narrow range from -0.6 to 0.6 g kg^{-1} . By comparison, the

range of changes in the wind field is much wider than in the moisture field. As a group, due to joint changes in the evolution of the low-level wind field and moisture field, the moisture transport evolution of these members in RadarDA becomes closer to that in OPT (Figs. 13a₂–e₂).

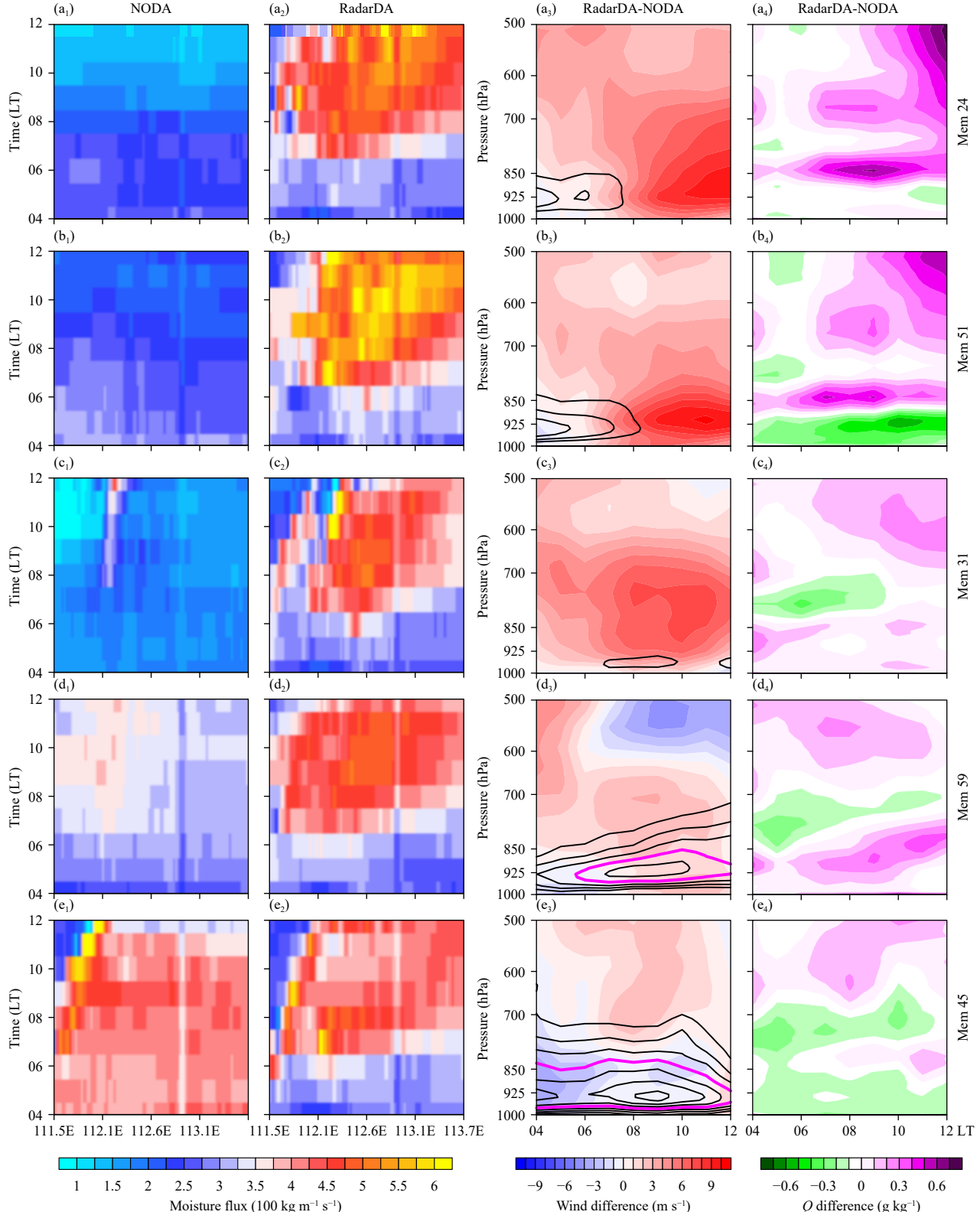


Fig. 13. Comparisons between (a₁–e₁) the five selected representative NODA members and (a₂–e₂) the corresponding RadarDA members: time–longitude plot of the vertically integrated (from the surface to 700 hPa) moisture flux ($100 \text{ kg m}^{-1} \text{ s}^{-1}$) across line AB in Fig. 9a during 0400–1200 LT 8 May 2013; (a₃–e₃) pressure–time plot of the averaged wind speed differences (shaded; m s^{-1}) across line AB in Fig. 9a between the five representative NODA members and the corresponding RadarDA members, and the wind speeds ($> 6 \text{ m s}^{-1}$, magenta line indicates 10 m s^{-1}) of five representative NODA members; and (a₄–e₄) pressure–time plot of the averaged specific humidity (Q) difference (shaded; g kg^{-1}) across line AB in Fig. 9a between the five representative NODA members and the corresponding RadarDA members.

Consequently, these members in RadarDA present convection evolution features that are very similar to those of the observations and OPT.

Generally, for most of the low-skill members, VrDA can reduce the initial wind-field error directly and the initial moisture-field error indirectly, and then, it can improve its presentation of the strength and direction of moisture transport. Thus, the convection can occur and develop at more accurate times and locations, and as a result, much better rainfall and convection evolution forecasts are produced. The improvement of forecast skill in most low-skill members results in improvement of the ensemble probability skill.

However, there is still some degree of uncertainty in the effect of VrDA. It is worth noting that VrDA helps improve the rainfall and convection evolution forecasts of most—but not all—members. After VrDA, the forecast skill (sum of 9-h AUC) of three members decreases rather than increases (Fig. 4). Except for the 39 members with improved FSS values, the remaining five low-score ($FSS < 0.3$) members have lower FSS values in RadarDA (Fig. 5). In other members, although the forecast skill scores are improved, the MCS evolution forecast becomes worse in RadarDA, such as in mem10 from the north sub-group (Figs. 4, 5, 14a). Compared to that in the OPT, the BL airflow in NODA mem10 has a similar wind direction but stronger wind speed (Fig. 15a₁), and the low-level moisture transport is also stronger during the forecast period (Fig. 15b₁). Thus, stronger convection occurs in the farther northwestern area with very similar evolution features, while the heavier rainfall belt with similar morphology is pushed towards the northwest in parallel (Fig. 14). Displacements of the MCS and rainfall locations explain the low skill. VrDA excessively decreases the intensity of the initial BL airflow in RadarDA mem10 (Fig. 15a₂). The subsequent evolution of the low-level moisture transport is rather different from that in the OPT (Fig. 15b₂), which causes the forecast error of convection evolution to grow with time. In such instances, an MCS with the wrong morphology moves rapidly southeastward (Figs. 14d₁–d₄).

EnKF data assimilation remains some uncertainties in improving the initial fields, and VrDA does not always improve the determinant forecast accuracy of ensemble members. When the adjusted initial fields have deviations from the optimal field that are slightly larger than the reasonable deviation range, such deviations will lead to much larger forecast errors (Zhang F. Q. et al., 2007; Zhang X. B. et al., 2016); thus, the forecast skill will decrease in minority members. This further proves that the practical predictability of the warm-sector HR is low, and

it is hard to accurately forecast warm-sector HR in southern China.

6. Summary and conclusions

Ensemble-based DA has been shown to help improve ensemble forecasts of severe convective weather (Roebber et al., 2004; Stensrud et al., 2009, 2013). Few studies have discussed how advanced ensemble-based DA approaches could improve ensemble forecasts of warm-sector HR over coastal southern China. On 8 May 2013, a warm-sector HR event influenced Yangjiang City in coastal southern China. Previous related studies have found that ensemble-probabilistic forecasts for this event have relatively poor accuracy. However, assimilating radial velocity from the Yangjiang radar with the EnKF approach can significantly improve probability forecasts (Bao et al., 2017). In this study, we performed two sets of 60-member ensemble experiments. One is conducted by using the Advanced WRF (WRF-ARW) model and lacks data assimilation (NODA), and the other cyclically assimilates radial velocity from the Yangjiang radar within 2 h at the early stage of this event through a WRF-based EnKF DA system (RadarDA). On this basis, we try to answer two major questions. (1) What are the characteristics and the reasons for the NODA ensemble-forecast errors of the warm-sector HR? (2) Why can the coastal radar radial-velocity ensemble assimilation improve the ensemble-forecast skill of the rainfall and convection evolution in this event?

The low-skill NODA ensemble members were classified into the poor forecast of rainfall amount group and the poor forecast of rainfall location group. The NODA ensemble-forecast errors of the warm-sector HR featured lower rainfall amounts or an inaccurate rainfall area. The speed and direction of the marine-BL southeasterly airflow from the northern part of southern China can influence the intensity and direction of low-level moisture transport, which plays a critical role in determining the time and location of the convection initiation as well as the intensity and location of the resultant rainfall. That is to say, an inaccurate marine-BL wind field could be the main reason for the forecast error of the rainfall and convection evolution.

Furthermore, the results show that cyclically assimilating coastal radar radial velocity in the early period of convection can lead to improved performance of the ensemble forecast of rainfall and convection in this event. Quantitative analysis results show that the forecast skill of the ensemble forecasts more than doubled after assimilation. The mean FSS of the 60 members greatly in-

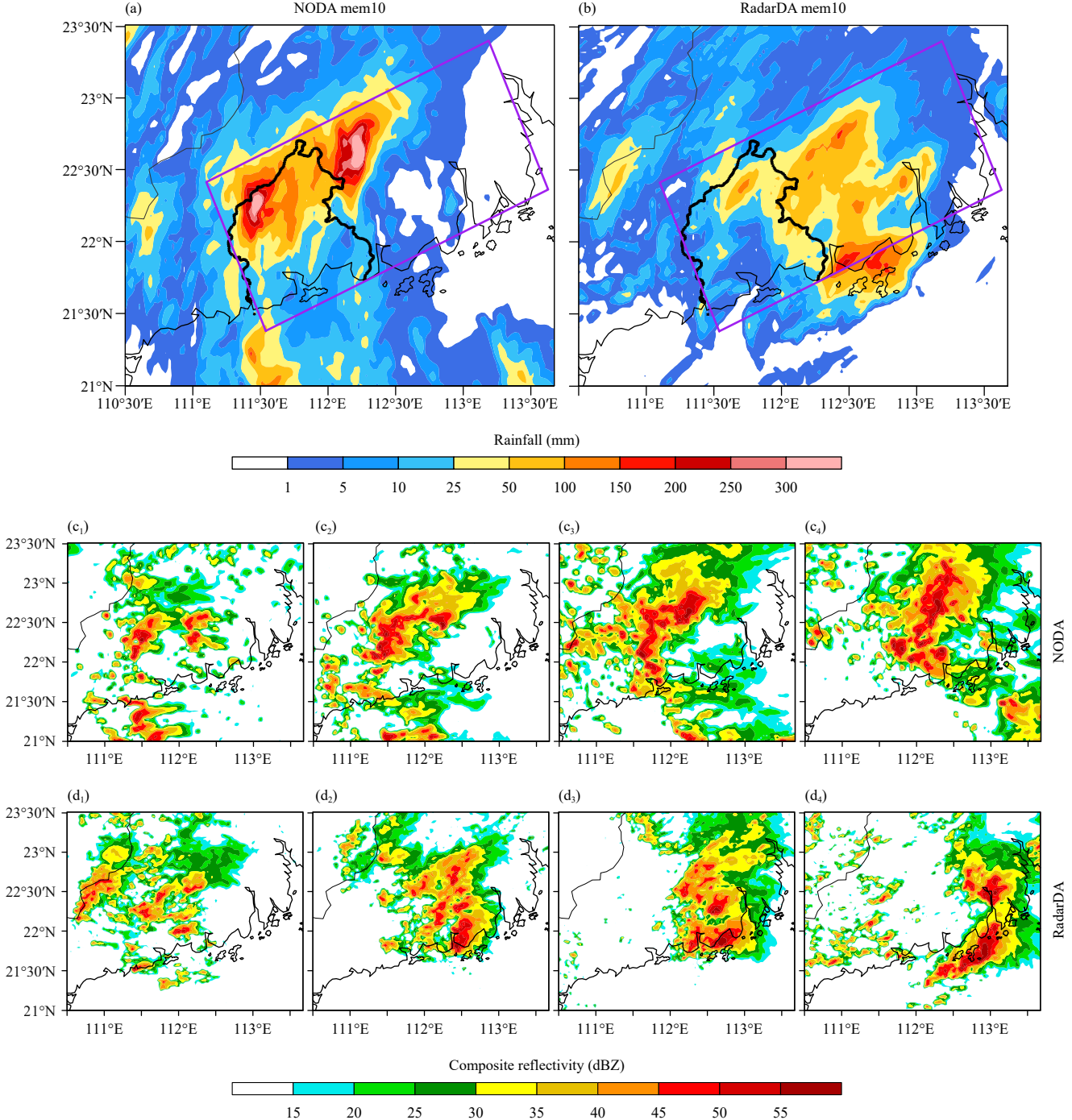


Fig. 14. Comparisons of rainfall accumulation during 0400–1200 LT 8 May 2013 between (a) NODA mem10 and (b) RadarDA mem10. The radar composite reflectivity (dBZ) from (c₁–c₄) NODA mem10 and (d₁–d₄) RadarDA mem10 every 2 hours during 0600–1200 LT 8 May 2013.

creases from 0.21 in NODA to 0.44 in RadarDA; meanwhile, the mean NEP averaged over the regions of an HR-producing MCS during the convection maturity stage (1000–1200 LT) sharply rises from 0.33 in NODA to 0.68 in RadarDA. After VrDA, the number of HR forecast skill ($FSS > 0.3$) members increased from 16 to 45, and 89% (39/44) of the low-scorre ($FSS < 0.3$) members presented various degrees of improvement in their rain-

fall forecast scores. Meanwhile, the forecast probabilities of the convection evolution greatly increased, despite slight displacement errors.

The improvement of the ensemble probability forecast skill depends on the improvement of the deterministic forecast skill of most members. VrDA can directly reduce the initial field errors of the wind speed and direction and indirectly make slight changes to the initial

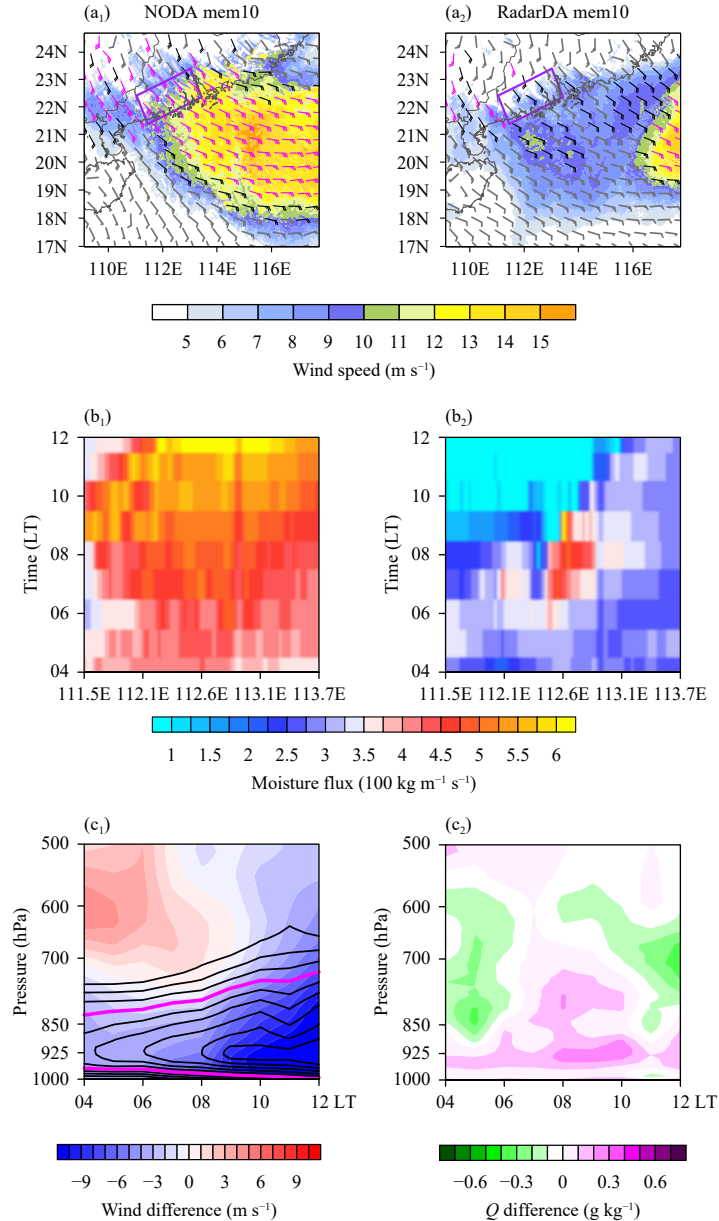


Fig. 15. Comparisons between NODA mem10 and RadarDA mem10: (a₁, a₂) the 950-hPa wind field (full barb = 5 m s⁻¹, magenta > 12 m s⁻¹, black = 10–12 m s⁻¹, and gray < 10 m s⁻¹) and wind speed (shaded; m s⁻¹); (b₁, b₂) time–longitude plot of the vertically integrated (from the surface to 700 hPa) moisture flux (100 kg m⁻¹ s⁻¹) across line AB in Fig. 9a during 0400–1200 LT 8 May 2013; (c₁) pressure–time plot of the averaged wind speed differences (shaded; m s⁻¹) across line AB between NODA mem10 and RadarDA mem10, and the wind speed (> 6 m s⁻¹, magenta line indicates 10 m s⁻¹) of NODA mem10; (c₂) pressure–time plot of the averaged specific humidity (Q) difference (shaded; g kg⁻¹) between NODA mem10 and RadarDA mem10 across line AB in Fig. 9a.

moisture field for most members. This leads to improvements in the evolution features of moisture transport during the subsequent forecast period. Thus, these members in RadarDA can better capture the formation and development of an MCS and have higher degrees of forecast skill for rainfall and convection evolution. It is thus clear that targeted assimilation of observations can reduce the critical model initial field errors and then efficiently improve ensemble forecasts of this low-predictability

warm-sector HR event over coastal southern China.

Notably, for some members, VrDA does not improve the performance of the deterministic forecast of rainfall or convection evolution. The comparison of a typical member between NODA and RadarDA shows that the small errors in the initial field caused by over-adjustments of the DA generate large forecast errors for convection evolution. On one hand, this indicates that the WRF-based EnKF DA system has some uncertainties in

improving the deterministic forecast of ensemble members. On the other hand, this further indicates that the warm-sector HR in coastal southern China has low practical predictability, and creating an accurate forecast for this type of event is very difficult.

Overall, the above conclusions are based only on a single case. In the future, studies on more cases are needed to further demonstrate the ability of VrDA with the EnKF method to improve the performance of ensemble forecasts on warm-sector HR in southern China.

Acknowledgments. This research is a part of the Southern China Monsoon Rainfall Experiment (SCM-REX), which is a Research and Development Project of the World Weather Research Programme (WWRP).

REFERENCES

- Bao, X. H., and S. N. Yang, 2015: Deterministic-prediction experiment of one torrential rainfall event in Southern China using a WRF-EnKF system. *Meteor. Mon.*, **41**, 566–576, doi: [10.7519/j.issn.1000-0526.2015.05.005](https://doi.org/10.7519/j.issn.1000-0526.2015.05.005). (in Chinese)
- Bao, X. H., Y. L. Luo, J. X. Sun, et al., 2017: Assimilating Doppler radar observations with an ensemble Kalman filter for convection-permitting prediction of convective development in a heavy rainfall event during the pre-summer rainy season of South China. *Sci. China Earth Sci.*, **60**, 1866–1885, doi: [10.1007/s11430-017-9076-9](https://doi.org/10.1007/s11430-017-9076-9).
- Bao, X. H., Y. L. Luo, and X. Y. Gao, 2021: The synoptic impacts on the convection initiation of a warm-sector heavy rainfall event over coastal South China prior to the monsoon onset: A numerical modeling study. *J. Geophys. Res. Atmos.*, **126**, e2020JD034335, doi: [10.1029/2020JD034335](https://doi.org/10.1029/2020JD034335).
- Barker, D. M., W. Huang, Y.-R. Guo, et al., 2004: A three-dimensional variational data assimilation system for MM5: Implementation and initial results. *Mon. Wea. Rev.*, **132**, 897–914, doi: [10.1175/1520-0493\(2004\)132<0897:ATVDAS>2.0.CO;2](https://doi.org/10.1175/1520-0493(2004)132<0897:ATVDAS>2.0.CO;2).
- Bjerknes, V., 1904: Das problem der Wettervorhersage, betrachtet vom Standpunkte der Mechanik und der Physik. *Meteor. Z.*, **21**, 1–7.
- Chen, F., and J. Dudhia, 2001: Coupling an advanced land surface-hydrology model with the Penn State-NCAR MM5 modeling system. Part I: Model implementation and sensitivity. *Mon. Wea. Rev.*, **129**, 569–585, doi: [10.1175/1520-0493\(2001\)129<0569:CAALSH>2.0.CO;2](https://doi.org/10.1175/1520-0493(2001)129<0569:CAALSH>2.0.CO;2).
- Compiling Group of Rainstorm in South China's Pre Flood Season, 1986: *Heavy Rainfall over Southern China in the Pre-summer Rainy Season*. Guangdong Science and Technology Press, Guangzhou, 244 pp. (in Chinese)
- Ding, Y. H., 1994: *Monsoons over China*. Kluwer Academic Publishers, Dordrecht, 419 pp.
- Du, J., and J. Chen, 2010: The corner stone in facilitating the transition from deterministic to probabilistic forecasts-ensemble forecasting and its impact on numerical weather prediction. *Meteor. Mon.*, **36**, 1–11, doi: [10.7519/j.issn.1000-0526.2010.11.001](https://doi.org/10.7519/j.issn.1000-0526.2010.11.001). (in Chinese)
- Du, Y., and G. X. Chen, 2018: Heavy rainfall associated with double low-level jets over southern China. Part I: Ensemble-based analysis. *Mon. Wea. Rev.*, **146**, 3827–3844, doi: [10.1175/MWR-D-18-0101.1](https://doi.org/10.1175/MWR-D-18-0101.1).
- Du, Y., and G. X. Chen, 2019: Heavy rainfall associated with double low-level Jets over southern China. Part II: Convection initiation. *Mon. Wea. Rev.*, **147**, 543–565, doi: [10.1175/MWR-D-18-0102.1](https://doi.org/10.1175/MWR-D-18-0102.1).
- Du, Y., G. X. Chen, B. Han, et al., 2020a: Convection initiation and growth at the coast of South China. Part I: Effect of the marine boundary layer jet. *Mon. Wea. Rev.*, **148**, 3847–3869, doi: [10.1175/MWR-D-20-0089.1](https://doi.org/10.1175/MWR-D-20-0089.1).
- Du, Y., G. X. Chen, B. Han, et al., 2020b: Convection initiation and growth at the coast of South China. Part II: Effects of the terrain, coastline, and cold pools. *Mon. Wea. Rev.*, **148**, 3871–3892, doi: [10.1175/MWR-D-20-0090.1](https://doi.org/10.1175/MWR-D-20-0090.1).
- Du, Y., Y. Shen, and G. X. Chen, 2022: Influence of coastal marine boundary layer jets on rainfall in South China. *Adv. Atmos. Sci.*, **39**, 782–801, doi: [10.1007/s00376-021-1195-7](https://doi.org/10.1007/s00376-021-1195-7).
- Dudhia, J., 1989: Numerical study of convection observed during the winter monsoon experiment using a mesoscale two-dimensional model. *J. Atmos. Sci.*, **46**, 3077–3107, doi: [10.1175/1520-0469\(1989\)046<3077:NSOCOD>2.0.CO;2](https://doi.org/10.1175/1520-0469(1989)046<3077:NSOCOD>2.0.CO;2).
- Feng, J., X. H. Qin, C. Q. Wu, et al., 2022: Improving typhoon predictions by assimilating the retrieval of atmospheric temperature profiles from the FengYun-4A's Geostationary Interferometric Infrared Sounder (GIIRS). *Atmos. Res.*, **280**, 106391, doi: [10.1016/j.atmosres.2022.106391](https://doi.org/10.1016/j.atmosres.2022.106391).
- Gao, X. Y., Y. L. Luo, Y. L. Lin, et al., 2022: A source of WRF simulation error for the early-summer warm-sector heavy rainfall over South China coast: Land-sea thermal contrast in the boundary layer. *J. Geophys. Res. Atmos.*, **127**, e2021JD035179, doi: [10.1029/2021JD035179](https://doi.org/10.1029/2021JD035179).
- Grell, G. A., and S. R. Freitas, 2014: A scale and aerosol aware stochastic convective parameterization for weather and air quality modeling. *Atmos. Chem. Phys.*, **14**, 5233–5250, doi: [10.5194/acp-14-5233-2014](https://doi.org/10.5194/acp-14-5233-2014).
- Hong, S.-Y., J. Dudhia, and S.-H. Chen, 2004: A revised approach to ice microphysical processes for the bulk parameterization of clouds and precipitation. *Mon. Wea. Rev.*, **132**, 103–120, doi: [10.1175/1520-0493\(2004\)132<0103:ARATIM>2.0.CO;2](https://doi.org/10.1175/1520-0493(2004)132<0103:ARATIM>2.0.CO;2).
- Huang, L., and Y. L. Luo, 2017: Evaluation of quantitative precipitation forecasts by TIGGE ensembles for South China during the presummer rainy season. *J. Geophys. Res. Atmos.*, **122**, 8494–8516, doi: [10.1002/2017JD026512](https://doi.org/10.1002/2017JD026512).
- Karstens, C. D., G. Stumpf, C. Ling, et al., 2015: Evaluation of a probabilistic forecasting methodology for severe convective weather in the 2014 Hazardous Weather Testbed. *Wea. Forecasting*, **30**, 1551–1570, doi: [10.1175/WAF-D-14-00163.1](https://doi.org/10.1175/WAF-D-14-00163.1).
- Li, X. Q., and Y. Du, 2021: Statistical relationships between two types of heavy rainfall and low-level jets in South China. *J. Climate*, **34**, 8549–8566, doi: [10.1175/JCLI-D-21-0121.1](https://doi.org/10.1175/JCLI-D-21-0121.1).
- Liu, X., Y. L. Luo, Z. Y. Guan, et al., 2018: An extreme rainfall event in coastal South China during SCMREX-2014: Formation and roles of rainband and echo trainings. *J. Geophys. Res. Atmos.*, **123**, 9256–9278, doi: [10.1029/2018JD028418](https://doi.org/10.1029/2018JD028418).
- Lorenz, E. N., 1963: Deterministic nonperiodic flow. *J. Atmos. Sci.*, **20**, 130–141, doi: [10.1175/1520-0469\(1963\)020<0130:DNF>2.0.CO;2](https://doi.org/10.1175/1520-0469(1963)020<0130:DNF>2.0.CO;2).
- Lorenz, E. N., 1969: The predictability of a flow which possesses many scales of motion. *Tellus*, **21**, 289–307, doi: [10.1111/j.1600-0889.1969.tb00453.x](https://doi.org/10.1111/j.1600-0889.1969.tb00453.x).

- [2153-3490.1969.tb00444.x](#).
- Lorenz, E. N., 1995: Predictability: A Problem Partly Solved. ECMWF Seminar on Predictability, Shinfield Park, Reading, 1–18.
- Luo, Y. L., and Y. R. X. Chen, 2015: Investigation of the predictability and physical mechanisms of an extreme-rainfall-producing mesoscale convective system along the Meiyu front in East China: An ensemble approach. *J. Geophys. Res. Atmos.*, **120**, 10,593–10,618, doi: [10.1002/2015JD023584](#).
- Luo, Y. L., R. D. Xia, and J. C. L. Chan, 2020: Characteristics, physical mechanisms, and prediction of pre-summer rainfall over South China: Research progress during 2008–2019. *J. Meteor. Soc. Japan*, **98**, 19–42, doi: [10.2151/jmsj.2020-002](#).
- Luo, Y. L., R. H. Zhang, Q. L. Wan, et al., 2017: The Southern China monsoon rainfall experiment (SCMREX). *Bull. Amer. Meteor. Soc.*, **98**, 999–1013, doi: [10.1175/BAMS-D-15-00235.1](#).
- Mason, S. J., and N. E. Graham, 1999: Conditional probabilities, relative operating characteristics, and relative operating levels. *Wea. Forecasting*, **14**, 713–725, doi: [10.1175/1520-0434\(1999\)014<0713:CPROCA>2.0.CO;2](#).
- Mason, S. J., and N. E. Graham, 2002: Areas beneath the relative operating characteristics (ROC) and relative operating levels (ROL) curves: Statistical significance and interpretation. *Quart. J. Roy. Meteor. Soc.*, **128**, 2145–2166, doi: [10.1256/003590002320603584](#).
- Meng, Z. Y., and F. Q. Zhang, 2007: Tests of an ensemble Kalman filter for mesoscale and regional-scale data assimilation. Part II: Imperfect model experiments. *Mon. Wea. Rev.*, **135**, 1403–1423, doi: [10.1175/MWR352.1](#).
- Meng, Z. Y., and F. Q. Zhang, 2008a: Tests of an ensemble Kalman filter for mesoscale and regional-scale data assimilation. Part III: Comparison with 3DVAR in a real-data case study. *Mon. Wea. Rev.*, **136**, 522–540, doi: [10.1175/2007MWR2106.1](#).
- Meng, Z. Y., and F. Q. Zhang, 2008b: Tests of an ensemble Kalman filter for mesoscale and regional-scale data assimilation. Part IV: Comparison with 3DVAR in a month-long experiment. *Mon. Wea. Rev.*, **136**, 3671–3682, doi: [10.1175/2008MWR2270.1](#).
- Mlawer, E. J., S. J. Taubman, P. D. Brown, et al., 1997: Radiative transfer for inhomogeneous atmospheres: RRTM, a validated correlated- k model for the longwave. *J. Geophys. Res. Atmos.*, **102**, 16,663–16,682, doi: [10.1029/97JD00237](#).
- Mu, M., 2013: Methods, current status, and prospect of targeted observation. *Sci. China Earth Sci.*, **56**, 1997–2005, doi: [10.1007/s11430-013-4727-x](#).
- Mu, M., W. S. Duan, and Y. M. Tang, 2017: The predictability of atmospheric and oceanic motions: Retrospect and prospects. *Sci. China Earth Sci.*, **60**, 2001–2012, doi: [10.1007/s11430-016-9101-x](#).
- Noh, Y., W. G. Cheon, S. Y. Hong, et al., 2003: Improvement of the K-profile model for the planetary boundary layer based on large eddy simulation data. *Bound.-Layer Meteor.*, **107**, 401–427, doi: [10.1023/A:1022146015946](#).
- Pan, Y. J., M. J. Wang, and M. Xue, 2020: Impacts of humidity adjustment through radar data assimilation using cloud analysis on the analysis and prediction of a squall line in southern China. *Earth Space Sci.*, **7**, e2019EA000893, doi: [10.1029/2019EA000893](#).
- Qin, X. J., W. S. Duan, P.-W. Chan, et al., 2023: Effects of dropsonde data in field campaigns on forecasts of tropical cyclones over the Western North Pacific in 2020 and the role of CNOP sensitivity. *Adv. Atmos. Sci.*, **40**, 791–803, doi: [10.1007/s00376-022-2136-9](#).
- Qiu, X. X., and F. Q. Zhang, 2016: Prediction and predictability of a catastrophic local extreme precipitation event through cloud-resolving ensemble analysis and forecasting with Doppler radar observations. *Sci. China Earth Sci.*, **59**, 518–532, doi: [10.1007/s11430-015-5224-1](#).
- Roberts, N. M., and H. W. Lean, 2008: Scale-selective verification of rainfall accumulations from high-resolution forecasts of convective events. *Mon. Wea. Rev.*, **136**, 78–97, doi: [10.1175/2007mwr2123.1](#).
- Roebber, P. J., D. M. Schultz, B. A. Colle, et al., 2004: Toward improved prediction: High-resolution and ensemble modeling systems in operations. *Wea. Forecasting*, **19**, 936–949, doi: [10.1175/1520-0434\(2004\)019<0936:TIPHAE>2.0.CO;2](#).
- Schwartz, C. S., J. S. Kain, S. J. Weiss, et al., 2010: Toward improved convection-allowing ensembles: Model physics sensitivities and optimizing probabilistic guidance with small ensemble membership. *Wea. Forecasting*, **25**, 263–280, doi: [10.1175/2009WAF2222267.1](#).
- Skamarock, W. C., J. B. Klpmp, J. Dudhia, et al., 2008: A Description of the Advanced Research WRF Version 3. NCAR/TN-475+STR, National Center for Atmospheric Research, Boulder, USA, 113 pp.
- Stensrud, D. J., M. Xue, L. J. Wicker, et al., 2009: Convective-scale warn-on-forecast system: A vision for 2020. *Bull. Amer. Meteor. Soc.*, **90**, 1487–1500, doi: [https://doi.org/10.1175/2009BAMS2795.1](#).
- Stensrud, D. J., L. J. Wicker, M. Xue, et al., 2013: Progress and challenges with Warn-on-Forecast. *Atmos. Res.*, **123**, 2–16, doi: [10.1016/j.atmosres.2012.04.004](#).
- Sun, X. Y., Y. L. Luo, X. Y. Gao, et al., 2021: On the localized extreme rainfall over the great bay area in South China with complex topography and strong UHI effects. *Mon. Wea. Rev.*, **149**, 2777–2801, doi: [10.1175/MWR-D-21-0004.1](#).
- Talagrand, O., 1997: Assimilation of observations, an introduction. *J. Meteor. Soc. Japan*, **75**, 191–209, doi: [10.2151/jmsj1965.75.1B_191](#).
- Wu, M. W., Y. L. Luo, F. Chen, et al., 2019: Observed link of extreme hourly precipitation changes to urbanization over coastal South China. *J. Appl. Meteor. Climatol.*, **58**, 1799–1819, doi: [10.1175/JAMC-D-18-0284.1](#).
- Wu, N. G., X. R. Zhuang, J. Z. Min, et al., 2020: Practical and intrinsic predictability of a warm-sector torrential rainfall event in the South China monsoon region. *J. Geophys. Res. Atmos.*, **125**, e2019JD031313, doi: [10.1029/2019JD031313](#).
- Wu, Y. L., Z. Q. Liu, and D. Q. Li, 2020: Improving forecasts of a record-breaking rainstorm in Guangzhou by assimilating every 10-min AHI radiances with WRF 4DVAR. *Atmos. Res.*, **239**, 104912, doi: [10.1016/j.atmosres.2020.104912](#).
- Yin, J. F., D.-L. Zhang, Y. L. Luo, et al., 2020: On the extreme rainfall event of 7 May 2017 over the coastal city of Guangzhou. Part I: Impacts of urbanization and orography. *Mon. Wea. Rev.*, **148**, 955–979, doi: [10.1175/mwr-d-19-0212.1](#).
- Yue, J., and Z. Y. Meng, 2017: Impact of assimilating Taiwan's

- coastal radar radial velocity on forecasting Typhoon Morakot (2009) in southeastern China using a WRF-based EnKF. *Sci. China Earth Sci.*, **60**, 315–327, doi: [10.1007/s11430-015-0259-y](https://doi.org/10.1007/s11430-015-0259-y).
- Yussouf, N., E. R. Mansell, L. J. Wicker, et al., 2013: The ensemble Kalman filter analyses and forecasts of the 8 May 2003 Oklahoma City tornadic supercell storm using single- and double-moment microphysics schemes. *Mon. Wea. Rev.*, **141**, 3388–3412, doi: [10.1175/MWR-D-12-00237.1](https://doi.org/10.1175/MWR-D-12-00237.1).
- Yussouf, N., D. C. Dowell, L. J. Wicker, et al., 2015: Storm-scale data assimilation and ensemble forecasts for the 27 April 2011 severe weather outbreak in Alabama. *Mon. Wea. Rev.*, **143**, 3044–3066, doi: [10.1175/MWR-D-14-00268.1](https://doi.org/10.1175/MWR-D-14-00268.1).
- Zhang, F. Q., and C. Snyder, 2007: Ensemble-based data assimilation. *Bull. Amer. Meteor. Soc.*, **88**, 565–568, doi: [10.1175/BAMS-88-4-565](https://doi.org/10.1175/BAMS-88-4-565).
- Zhang, F. Q., Z. Y. Meng, and A. Aksoy, 2006: Tests of an ensemble Kalman filter for mesoscale and regional-scale data assimilation. Part I: Perfect model experiments. *Mon. Wea. Rev.*, **134**, 722–736, doi: [10.1175/MWR3101.1](https://doi.org/10.1175/MWR3101.1).
- Zhang, F. Q., N. F. Bei, R. Rotunno, et al., 2007: Mesoscale predictability of moist baroclinic waves: Convection-permitting experiments and multistage error growth dynamics. *J. Atmos. Sci.*, **64**, 3579–3594, doi: [10.1175/JAS4028.1](https://doi.org/10.1175/JAS4028.1).
- Zhang, F. Q., Y. H. Weng, J. A. Sippel, et al., 2009: Cloud-resolving hurricane initialization and prediction through assimilation of Doppler radar observations with an ensemble Kalman filter. *Mon. Wea. Rev.*, **137**, 2105–2125, doi: [10.1175/2009MWR2645.1](https://doi.org/10.1175/2009MWR2645.1).
- Zhang, M. R., and Z. Y. Meng, 2019: Warm-Sector heavy rainfall in southern China and its WRF simulation evaluation: A low-level-jet perspective. *Mon. Wea. Rev.*, **147**, 4461–4480, doi: [10.1175/MWR-D-19-0110.1](https://doi.org/10.1175/MWR-D-19-0110.1).
- Zhang, X. B., Y. L. Luo, Q. L. Wan, et al., 2016: Impact of assimilating wind profiling radar observations on convection-permitting quantitative precipitation forecasts during SCMREX. *Wea. Forecasting*, **31**, 1271–1292, doi: [10.1175/WAF-D-15-0156.1](https://doi.org/10.1175/WAF-D-15-0156.1).
- Zhang, Y. J., and F. Q. Zhang, 2018: A review on the ensemble-based data assimilations for severe convective storms. *Adv. Meteor. Sci. Technol.*, **8**, 38–52, doi: [10.3969/j.issn.2095-1973.2018.03.003](https://doi.org/10.3969/j.issn.2095-1973.2018.03.003). (in Chinese)
- Zhu, L., Q. L. Wan, X. Y. Shen, et al., 2016: Prediction and predictability of high-impact western Pacific landfalling Tropical Cyclone Vicente (2012) through convection-permitting ensemble assimilation of Doppler radar velocity. *Mon. Wea. Rev.*, **144**, 21–43, doi: [10.1175/MWR-D-14-00403.1](https://doi.org/10.1175/MWR-D-14-00403.1).